Monthly Notices of the ROYAL ASTRONOMICAL SOCIETY

MNRAS **500,** 1476–1490 (2021) doi:10.1093/mnras/staa3203
Advance Access publication 2020 October 16

The changing circumgalactic medium over the last 10 Gyr – I. Physical and dynamical properties

Ezra Huscher,[1]★ Benjamin D. Oppenheimer,[1,2]★ Alice Lonardi,[1] Robert A. Crain,[3] Alexander J. Richings[4] and Joop Schaye[5]

[1]*CASA, Department of Astrophysical and Planetary Sciences, University of Colorado, 389 UCB, Boulder, CO 80309, USA*
[2]*Harvard-Smithsonian Center for Astrophysics, 60 Garden St, Cambridge, MA 02138, USA*
[3]*Astrophysics Research Institute, Liverpool John Moores University, 146 Brownlow Hill, Liverpool L3 5RF, UK*
[4]*Institute for Computational Cosmology, Durham University, South Road, Durham DH1 3LE, UK*
[5]*Leiden Observatory, Leiden University, P.O. Box 9513, NL-2300 RA Leiden, The Netherlands*

Accepted 2020 September 23. Received 2020 August 30; in original form 2020 May 12

ABSTRACT

We present an analysis of the physical and dynamical states of two sets of EAGLE zoom simulations of galaxy haloes, one at high redshift ($z = 2-3$) and the other at low redshift ($z = 0$), with masses of $\approx 10^{12}$ M$_\odot$. Our focus is how the circumgalactic medium (CGM) of these L^* star-forming galaxies change over the last 10 Gyr. We find that the high-z CGM is almost equally divided between the 'cool' ($T < 10^5$ K) and 'hot' ($T \geq 10^5$ K) phases, while at low-z the hot CGM phase contains 5 × more mass than the cool phase. The high-z hot CGM contains 60 per cent more metals than the cool CGM, while the low-z cool CGM contains 35 per cent more metals than the hot CGM. The metals are evenly distributed radially between the hot and cool phases throughout the high-z CGM. At high z, the CGM volume is dominated by hot outflows, but also contains cool gas mainly inflowing and cool metals mainly outflowing. At low z, the cool metals dominate the interior and the hot metals are more prevalent at larger radii. The low-z cool CGM has tangential motions consistent with rotational support out to $0.2R_{200}$, often exhibiting $r \approx 40$ kpc disc-like structures. The low-z hot CGM has several times greater angular momentum than the cool CGM, and a more flattened radial density profile than the high-z hot CGM. This study verifies that, just as galaxies demonstrate significant transformations over cosmic time, the gaseous haloes surrounding them also undergo considerable changes of their own both in physical characteristics of density, temperature, and metallicity, and dynamic properties of velocity and angular momentum.

Key words: methods: numerical – galaxies: evolution – galaxies: formation – galaxies: haloes – galaxies: high-redshift – intergalactic medium.

1 INTRODUCTION

It is well established that galaxies are surrounded by gaseous reservoirs of baryons and metals extending far beyond the optical stellar component. Observational probes of a galaxy's circumgalactic medium (CGM) span across cosmic time from the relatively local Universe (e.g. Tumlinson et al. 2011; Stocke et al. 2013; Borthakur et al. 2015; Burchett et al. 2015; Johnson, Chen & Mulchaey 2015) to the peak of cosmic star formation (e.g. Adelberger et al. 2003; Steidel et al. 2010; Turner et al. 2014; Gatkine, Veilleux & Cucchiara 2019; Rudie et al. 2019) and beyond. While galaxies change dramatically in appearance from the *high-redshift* epoch, sometimes referred to as 'Cosmic Noon' ($z \approx 2-3$), to comparatively nearby *low-redshift* galaxies ($z \lesssim 0.3$), it is less well understood how the CGM of these galaxies change.

Galaxies evolve dramatically in appearance from high to low redshift. If one selects halo masses at both epochs that provide the most efficient conversion of baryons to stars, $M_{\rm halo} \sim 10^{12}$ M$_\odot$ (Behroozi, Wechsler & Conroy 2013a), the central galaxies predicted to inhabit them are dramatically different. Galaxies at high-z are forming stars in excess of 10 × the present-day rate (Pettini et al. 2001). They are also more compact (van Dokkum et al. 2008) and their morphologies more asymmetric (Abraham et al. 1996), despite having similar stellar masses (Behroozi, Wechsler & Conroy 2013b; Moster, Naab & White 2013).

Comparing the CGM across 10 Gyr of cosmic time (i.e. from $z = 3$ to $z = 0$) has not received the same attention as galaxies, but absorption line measurements of the same species do exist at both epochs. Chen (2012) compared the UV absorption line probes of the CGM at $z \approx 0.1$ and $z \approx 2.2$ finding that the spatial extent and mean absorption strengths of UV transitions change little over 10 Gyr of evolution around similar mass galaxies. A comparison of column densities of a variety of UV absorption species around star-forming L^* haloes between Werk et al. (2013) at $z \sim 0.2$ and Rudie et al. (2019) at $z \approx 2$ finds similar column densities as a function of physical separation (i.e. physical not comoving kpc).

While comparing the low-z and high-z CGM is now possible due to growing observational data bases at both epochs, it is also necessary to use sophisticated theoretical tools to contrast the physical properties of gaseous haloes across time. Cosmological

★ E-mail: ezra.huscher@colorado.edu (EH); benjamin.oppenheimer@colorado.edu (BDO)

hydrodynamic simulation codes have been developed that reproduce crucial properties of galaxy populations at both low and high redshift, including the Evolution and Assembly of GaLaxies and their Environments (EAGLE; Schaye et al. 2015), Illustris-TNG (Pillepich et al. 2018), Horizon-active galactic nuclei (AGN; Dubois et al. 2016), and SIMBA (Davé et al. 2019) simulations. These simulation suites apply detailed modules for a variety of processes associated with galaxy formation, including gas cooling, star formation, the growth of supermassive black holes (SMBHs), and stellar and SMBH superwind feedback. EAGLE is not calibrated to reproduce observations of gas (Crain et al. 2015), but other suites have been calibrated against some gas observations (e.g. Pillepich et al. 2018). Therefore, EAGLE provides genuine predictions for the physical and observational characteristics of the CGM.

In this paper, we expand upon a set of high-resolution, cosmological zoom simulations called the EAGLE–CGM Project introduced by Oppenheimer et al. (2016, hereafter O16) using the EAGLE prescription. These simulations ran at higher resolution than the main EAGLE volume and integrated non-equilibrium (NEQ) ionization and cooling for diffuse gas introduced in Oppenheimer & Schaye (2013) and integrated in the CHIMES NEQ chemistry and cooling module developed by Richings, Schaye & Oppenheimer (2014). We complement the original set of zoom simulations reaching typical halo masses of $M_{200} = 10^{12}\,\mathrm{M}_\odot$ by the $z \lesssim 0.3$ epoch with a set of high-z ($z = 2{-}3$) galaxy haloes also with $M_{200} = 10^{12}\,\mathrm{M}_\odot$, where M_{200} is the mass enclosed within a sphere with mean density of $200\times$ the critical density. These high-z haloes are the progenitors of low-redshift EAGLE–CGM zooms of $M_{200} \sim 10^{13}\,\mathrm{M}_\odot$ haloes, often hosting passive galaxies at $z \leq 0.2$.

This paper is the first of a series of papers investigating the CGM at similar halo mass across different epochs. Here, we compare the physical and kinematic properties of gaseous haloes hosting galaxies that are most efficient at turning their baryons into stars. At low redshift, these are disc galaxies, often with 'grand design' spiral morphologies, with typical $M_* = 1{-}3\times10^{10}\,\mathrm{M}_\odot$ and SFR $= 0.5{-}3.0\,\mathrm{M}_\odot\,\mathrm{yr}^{-1}$. At high-redshift, these galaxies have similar stellar masses, $M_* = 0.6{-}3\times10^{10}\,\mathrm{M}_\odot$ but with SFR $= 5{-}45\,\mathrm{M}_\odot\,\mathrm{yr}^{-1}$, which are consistent with the properties of Lyman-Break Galaxies (Steidel et al. 1996).

We aim to compare and contrast several fundamental properties of star-forming galaxies occupying $10^{12}\,\mathrm{M}_\odot$ haloes across cosmic time. These include the gaseous mass budget within haloes, divided into categories of cool (defined here at $T < 10^5$ K), hot ($T > 10^5$ K), and interstellar (defined as star forming) in Section 3.1. We also consider the metal contents and metallicities of gaseous haloes in Section 3.2. The velocities of cool and hot CGM components are compared across epochs in Section 3.3. In Section 3.4, we compare the angular momenta of the CGM components, including the relative angles of their axes. Lastly, we present hot gas radial profiles in Section 3.5.

We emphasize that the low-z EAGLE–CGM haloes have been well tested against observational data sets of UV ions. Oppenheimer et al. (2018b) found good agreement for a number of low metal ions observed by COS–Haloes (Werk et al. 2013), including C II, Si II, Si III, and Si IV, but underproduced the observed Mg II strengths. O16 reproduced the observed correlation between specific star formation rate (sSFR) and O VI (Tumlinson et al. 2011), but underpredicted their column densities, which Oppenheimer et al. (2018a) later argued could be enhanced to observed levels by flickering AGN flash-ionizing the CGM and leaving metals overionized long after the AGN turns off. In a companion paper (Lonardi et al., in preparation), we will show that the high-z zoom haloes broadly reproduce the observed column densities of Rudie et al. (2019). This series of papers contrasting the two selected epochs relies on testing our simulations against observations using ion-by-ion tracking of the NEQ module (Oppenheimer & Schaye 2013; Richings et al. 2014).

The paper is organized as follows. In Section 2, we review the code used for EAGLE–CGM simulations and introduce our set of simulations. The main results are presented in Section 3 on topics of CGM mass (Section 3.1), metals (Section 3.2), velocities (Section 3.3), and angular momentum (Section 3.4), as well as hot gas profiles (Section 3.5). We discuss several findings in detail in Section 4. We summarize in Section 5. Physical kpc units are used throughout.

2 METHODS

2.1 The EAGLE simulation code

We introduce the simulations in this section, and refer the reader to section 2 of O16 for further details. We employ the EAGLE hydrodynamic simulation code introduced in Schaye et al. (2015), which uses the GADGET-3 N-body+SPH code (see Springel 2005), plus extensive modifications to simulate galaxy formation described below. The Planck Collaboration XVI (2014) cosmological parameters are adopted: $\Omega_\mathrm{m} = 0.307$, $\Omega_\Lambda = 0.693$, $\Omega_b = 0.04825$, $H_0 = 67.77\,\mathrm{km\,s^{-1}\,Mpc^{-1}}$, $\sigma_8 = 0.8288$, and $n_\mathrm{s} = 0.9611$. EAGLE applies the Hopkins (2013) pressure–entropy SPH formulation using a C2 Wendland (1995) 58-neighbour kernel along with several other hydrodynamic modifications collectively referred to as 'Anarchy' [appendix A of Schaye et al. (2015) and Schaller et al. (2015)].

The EAGLE simulations include subgrid prescriptions for radiative cooling (Wiersma, Schaye & Smith 2009a), star formation (Schaye & Dalla Vecchia 2008), stellar evolution and chemical enrichment (Wiersma et al. 2009b), and superwind feedback associated with star formation (Dalla Vecchia & Schaye 2012) and black hole growth (Schaye et al. 2015; Rosas-Guevara et al. 2016). The parameters governing the efficiency of the star formation feedback were calibrated to reproduce the present-day stellar masses of galaxies, whilst also recovering galaxy discs with realistic sizes. Those governing feedback associated with black hole growth were calibrated to reproduce the present-day relationship between the stellar mass of galaxies and the mass of their central black holes. The feedback calibration strategy is discussed in detail by Crain et al. (2015).

2.2 EAGLE zoom simulations

We analyse two samples of haloes, one at high z with redshifts ranging from $z = 2.24$ to 3.02 at halo masses from $M_{200} = 10^{11.90}$ to $10^{12.18}\,\mathrm{M}_\odot$, and one at $z = 0$ with $M_{200} = 10^{11.85}$ to $10^{12.28}\,\mathrm{M}_\odot$. We list these haloes in Table 1, and use identifiers of 'HiZ00X' and 'LoZ00X' for the individual haloes, where X is the halo number. The LoZ00X haloes are the same haloes listed in table 1 of O16 as 'Gal00X', but with values listed at $z = 0$ as opposed to $z = 0.205$ in that paper. The HiZ00X haloes are virialized haloes selected from the 'Grp00X' zooms listed in the same O16 table, but selected to have a $M_{200} \sim 10^{12}\,\mathrm{M}_\odot$ halo at high z. Hence, we are comparing to virialized progenitors of $M_{200} \sim 10^{13}\,\mathrm{M}_\odot$ $z = 0$ haloes.

The LoZ haloes are selected from the EAGLE Recal-L025N0752 simulation, and rerun with NEQ ionization and cooling CHIMES module developed by Richings et al. (2014) starting at $z = 0.503$. These are identical to the runs listed in O16, and have the *M5.3* resolution of O16 corresponding to an SPH particle mass

Table 1. Zoom simulations.

Halo	Mass sums within R_{200} for high-z haloes z	$M^a_{\rm cool}$	$M^a_{\rm hot}$	$M^a_{\rm CGM}$	M^a_{200}	$\frac{M_{\rm CGM}}{M_{200}}\frac{\Omega_m}{\Omega_b}{}^b$	Halo	Mass sums within R_{200} for low-z haloes z	$M^a_{\rm cool}$	$M^a_{\rm hot}$	$M^a_{\rm CGM}$	M^a_{200}	$\frac{M_{\rm CGM}}{M_{200}}\frac{\Omega_m}{\Omega_b}{}^b$
HiZ000	3.02	1.79	2.49	4.28	115	0.24	LoZ001	0	1.47	6.89	8.36	129	0.41
HiZ002	2.24	2.94	2.43	5.37	100	0.34	LoZ002	0	0.57	11.50	12.10	191	0.40
HiZ003	2.24	3.50	3.90	7.40	96	0.49	LoZ003	0	2.21	9.61	11.80	151	0.50
HiZ004	3.02	2.76	4.90	7.67	151	0.32	LoZ004	0	1.25	5.07	6.32	105	0.38
HiZ005	2.01	2.86	3.66	6.52	110	0.38	LoZ005	0	2.34	15.20	17.50	170	0.66
HiZ006	3.02	1.63	1.40	3.03	79	0.24	LoZ006	0	0.54	4.73	5.26	87	0.38
HiZ007	2.24	2.58	2.29	4.87	83	0.37	LoZ007	0	2.97	4.85	7.81	71	0.70
HiZ008	3.02	2.38	4.05	6.43	145	0.28	LoZ008	0	0.93	3.89	4.83	72	0.42
HiZ009	3.02	2.78	4.24	7.02	115	0.39	LoZ009	0	0.65	3.47	4.11	76	0.34
Averages:	2.63	2.58	3.26	5.84	110	0.34	Averages:	0	1.44	7.25	8.68	117	0.47

Notes. [a] $M_{\rm cool}$ ($M_{\rm hot}$) includes CGM gas at $<10^5$ ($\geq 10^5$) K. $M_{\rm CGM} = M_{\rm cool} + M_{\rm hot}$. In units of $10^{10}\,{\rm M}_\odot$.
[b] The fraction of a halo's cosmic proportion of baryons residing in the CGM inside R_{200}.

$m_{\rm SPH} = 2.2 \times 10^5\,{\rm M}_\odot$, using the notation $M[\log(m_{\rm SPH}/{\rm M}_\odot)]$. O16 demonstrated that these low-z haloes follow the M_* and sSFR relations of the Recal-L025N0752 simulation, and argued that these haloes are generalizable to the larger population of haloes hosting L^* star-forming galaxies in this 25^3 Mpc^3 simulation.

The HiZ haloes are originally selected from the EAGLE Ref-L100N1504, 100^3 Mpc^3 volume and also use the *M5.3* resolution. However, we re-ran all of these simulations using the NEQ module beginning at $z = 4$ to follow the haloes to at least the redshift listed in Table 1. We describe the NEQ module in Lonardi et al. (in preparation) when we present CGM ion column densities, but note here that O16 found no significant differences in physical or dynamical halo properties compared to runs evolved with cooling rates in chemical equilibrium. All simulations in this paper use a Plummer-equivalent softening length of 350 proper pc at $z < 2.8$, and 1.33 comoving kpc at $z > 2.8$. All zooms have the same resolution as the EAGLE Recal-L025N0752 run. There does not exist a statistical sample of high-z $\approx 10^{12}$ M$_\odot$ haloes in the Recal-L025N0752 volume to test how representative these haloes are, but O16 did argue that their $z = 0$ descendants exhibit typical galaxy properties compared to the lower resolution Ref-L100N1504 simulation.

2.3 Definition of temperature and ISM phases

Throughout, we divide gas into 'cool' and 'hot' phases using a temperature cut-off 10^5 K. Often gas in the $T = 10^{5-7}$ K range is considered 'warm–hot', with 'hot' being reserved for $>10^6$ K gas. The main reason we use a 10^5 K cut is because it divides cool gas, which is often in thermal equilibrium with the metagalactic UV background, from gas that is often heated to the virial temperature of the halo, which is $T_{\rm vir} \approx 10^6$ K for our haloes as shown in Fig. 1. Correa et al. (2018) explored the cooling properties of halo gas in the main EAGLE 100 Mpc simulation, and also found that $T = 10^5$ K represents a clear division between cool and hot gas in 10^{12} M$_\odot$ haloes with little gas around 10^5 K indicating that the cool–hot division is relatively insensitive to the precise temperature cut. We apply this cut additionally because UV photoionized absorption lines correspond to gas at $T \lesssim 10^5$ K (e.g. Ford et al. 2013; Rahmati et al. 2016).

We define the interstellar medium (ISM) as any gas with either (1) non-zero SFR or (2) a gas density threshold greater than $n_{\rm H} = 10^{-1}{\rm cm}^{-3}$. This specific definition is meant to exclude the cool ISM in the first case and neutral ISM in the second case. Using only the first criterion results in insignificant changes to CGM masses. The high-z, cool CGM metallicity profile we show in Fig. 7 is most sensitive to the ISM criteria. Adding the density threshold as a second criterion raises the cool, high-z CGM metallicity inside $0.3R_{200}$ by a factor of up to 2 versus the SFR-only criterion, where R_{200} is the radius of the sphere containing M_{200}. This owes to gas with $n_{\rm H} > 10^{-1}{\rm cm}^{-3}$ being metal poor and below the EAGLE star formation density criterion. EAGLE's star formation threshold is meant to simulate the transition from atomic to molecular phases, and hence the star formation density threshold increases with decreasing metallicity.

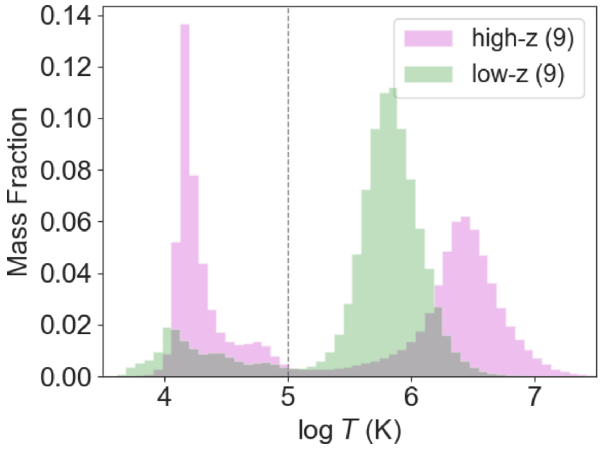

Figure 1. Normalized temperature distribution of CGM gas out to R_{200} in all nine high-z haloes (pink) and all nine low-z haloes (green). The temperature division we have chosen to separate hot and cool gas (10^5 K) is denoted with a dotted line.

3 PHYSICAL PROPERTIES OF HALOES

We begin this section by showing two representative 10^{12} M$_\odot$ haloes in Fig. 2, one at high z (HiZ009; left) and the other at low z (LoZ004; right) in density ($n_{\rm H}$), temperature (T), and metallicity (Z; from upper to lower panels). Both haloes are normalized to the virial radius, which is physically 2.5 × smaller for the $z = 3.02$ halo (213 versus 80 kpc). More dense, cool gas extends throughout the halo at high z, while this gas organizes itself into a disc structure extending nearly 100 kpc across at $z = 0$. At high z, the cool, dense gas is less metal enriched, which suggests that it is associated with cold accretion flows (e.g. Kereš et al. 2005, 2009; Dekel & Birnboim 2006; van

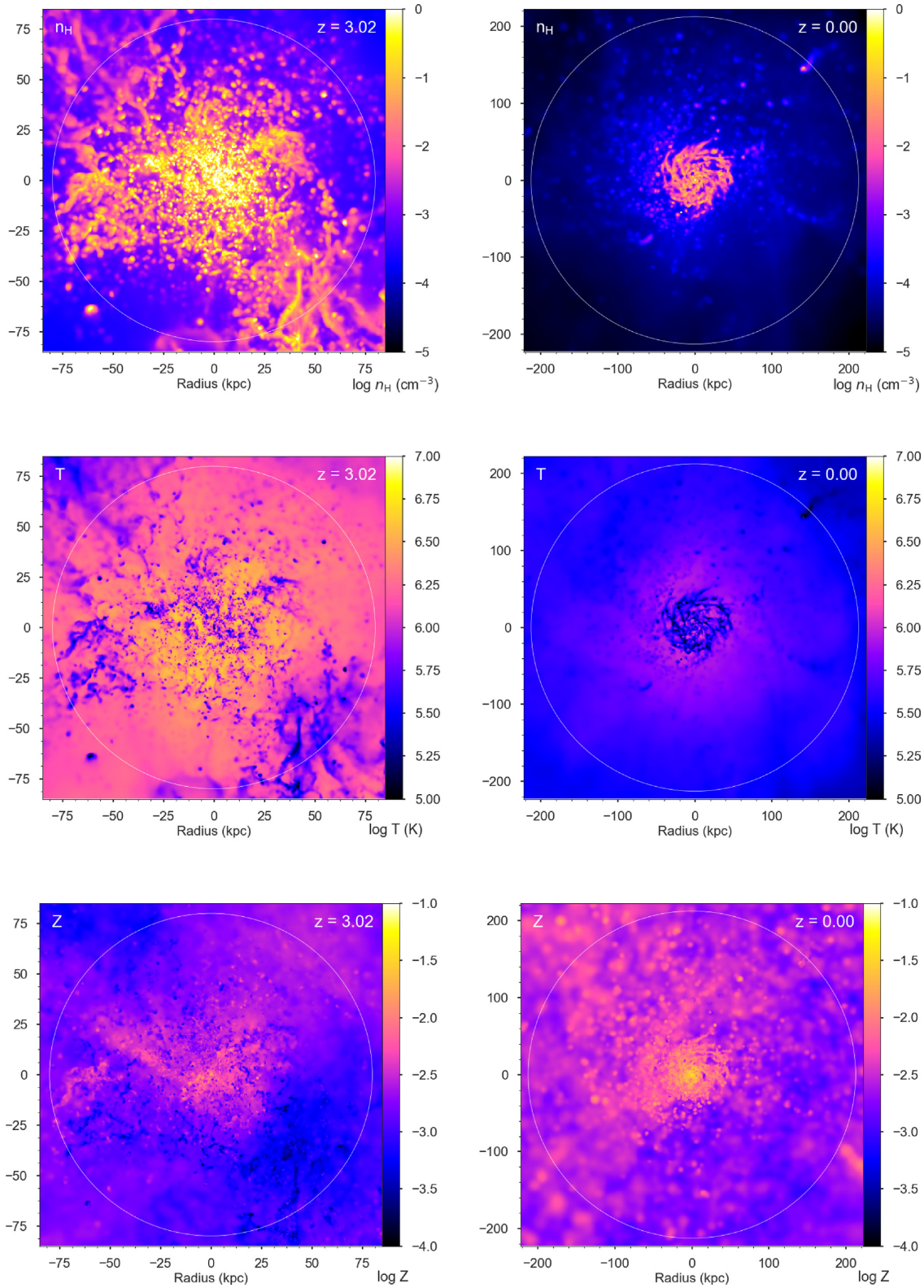

Figure 2. The physical properties of two 10^{12} $M_\odot$ haloes, HiZ009 on left and LoZ004 on right, plotted out to R_{200}, indicated by the white circles. From top to bottom, the panels show hydrogen number density, temperature, and absolute metallicity.

de Voort & Schaye 2012). At low z, the cool, dense gas appears more metal enriched in the disc structure. The volume-filling, hot gas medium is hotter at high z than at low z, which is to be expected given that the virial temperature scales with R_{200}^{-1} at fixed mass, resulting in a temperature scale $\sim$2.5 $\times$ higher at $z = 3$ However, we also see that the hotter gas is more often coincident with metal enrichment at high z, which suggests hot, enriched outflows are more common throughout the high-z CGM. These visual trends

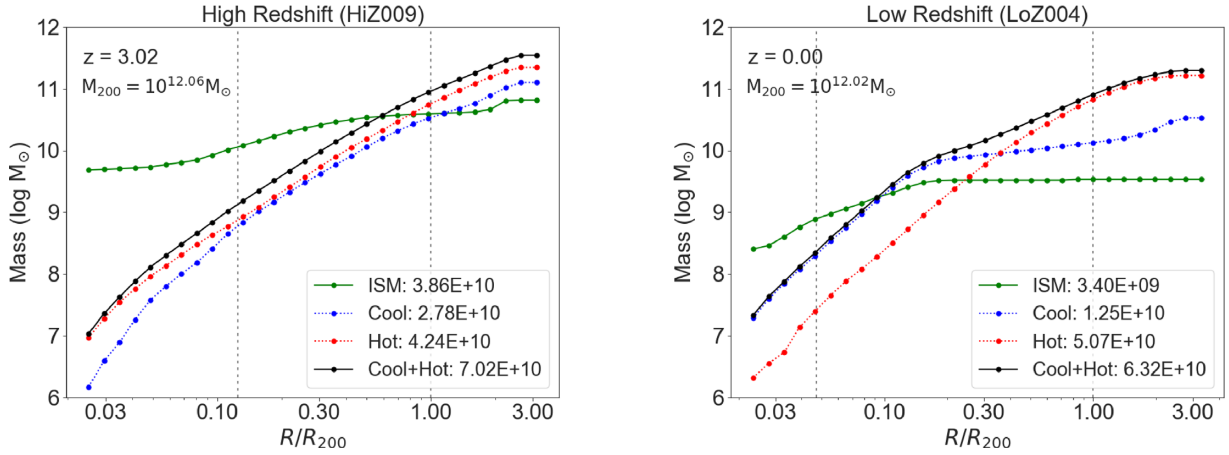

Figure 3. Cumulative mass as a function of normalized radius for gaseous components in two $M_{200} = 10^{12}\,M_\odot$ haloes, one at $z = 3$ (HiZ009; left) and one at $z = 0$ (LoZ004; right). ISM gas is green, cool CGM gas ($T < 10^5$ K) is blue, hot CGM gas ($T \geq 10^5$ K) is red, and the total sum is black. Legends show total masses out to R_{200}. Two vertical dashed lines indicate 10 physical kpc and R_{200}. The ratio of hot to cool CGM is much higher at low z by R_{200}, though the cool phase dominates in the interior of low-z haloes. The ISM gas is a much smaller fraction of the low-z total halo gas content than at high z. Note that a few neighbouring galaxies are found in these simulations, as seen here in the ISM increase of HiZ009 at $2R_{200}$.

prelude the quantitative results we demonstrate in the following subsections.

3.1 Mass

Fig. 3 plots the cumulative gas masses for our representative high-z and low-z haloes as a function of galactocentric radius R normalized by R_{200}. The integrated gas masses within R_{200} are listed in the legend. The green lines indicate the cumulative ISM gas mass, which is 11 $\times$ higher for the high-z halo ($3.9 \times 10^{10}\,M_\odot$ versus $3.4 \times 10^9\,M_\odot$), and is reflected in the SFR of these galaxies being 30 $\times$ different ($23.5\,M_\odot\,yr^{-1}$ versus $0.8\,M_\odot\,yr^{-1}$). The total CGM masses represented by black lines are more similar between the two haloes (7.0 versus $6.3 \times 10^{10}\,M_\odot$), but the division between the cool (the blue lines) and hot (the red lines) phases is rather different. Cool and hot phases nearly balance each other throughout the CGM at high z, but by low z the inner CGM is dominated by cool gas and the outer CGM by hot gas, which becomes the dominant phase throughout the low-z CGM out to R_{200}.

We generalize these results in Fig. 4, which shows the differential division between the cool and hot CGM across each sample of 9 high-z and low-z haloes. Cool gas accounts for the majority of the inner CGM of low-z haloes, but rapidly transitions to hot gas dominating at larger radii (and hot gas dominating the cumulative CGM mass out to R_{200}). In contrast, the high-z CGM appears less sorted by temperature phases, but retains a similar progression of cool gas being more dominant in the interior. The 'balance point' where the cool and hot CGM masses at a radius equal each other is $0.5R_{200}$ at high z and $0.2R_{200}$ at low z. Beyond R_{200}, the cool phase makes a comeback as the extended IGM gas is cooler.

3.2 Metals

We now turn our attention to the gaseous metal content of haloes. In Fig. 5, we plot the cumulative metallicity analogous to the mass accumulation of Fig. 3 for our representative haloes. At high z, we see hot metals in greater abundance than cool metals at every point in the halo all the way out to $3R_{200}$. In the next subsection, we will show that superwind feedback is pushing out metals in strong, hot

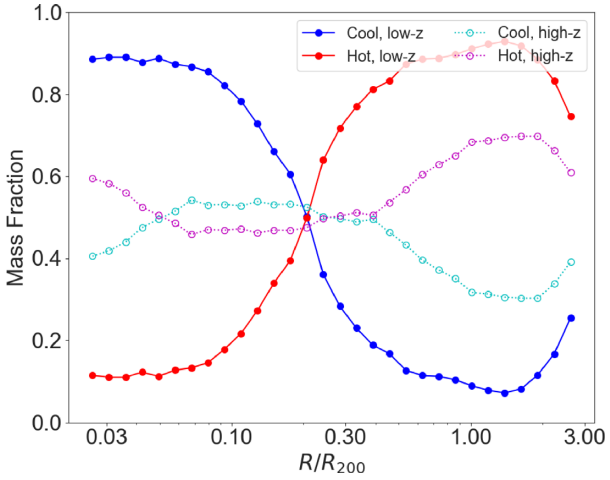

Figure 4. Average differential mass fractions across the nine high-z (dotted) and nine low-z haloes (solid), divided into hot and cool gas at 10^5K. At high redshift, cyan (magenta) indicates cool (hot) gas. At low redshift, blue (red) indicates cool (hot) gas. Cool (hot) gas dominates in the interior (exterior) of low-z haloes. High-z haloes have a much more even balance of cool and hot phases throughout the CGM. The turnover at $\approx 2R_{200}$ and beyond indicates more cool gas in structures extending outside the CGM and transitioning to the IGM.

outflows at high z. In contrast, cool metals dominate out to $0.5R_{200}$ in low-z haloes, and then give way to hotter metals beyond $0.5R_{200}$ when plotting differential fractions on a linear scale in Fig. 6.

By R_{200}, we see that the ISM holds nearly 50 per cent more metals than the galaxy's halo at high z (cf. the green and black lines in left-hand panel of Fig. 5). At low z, the CGM metals overcome the ISM metal content by $0.6R_{200}$ and have over 2.5 $\times$ the ISM metal content by R_{200}.

In Fig. 7, we plot the absolute metallicity (Z) of the CGM phases. Starting with cool metals, we see a 2−5 $\times$ greater mean Z at low z compared to high z, with a separation that grows at larger radii (left-hand panel). While the average low-z metallicity approaches solar in the interior (Asplund et al. 2009, $Z_\odot \equiv 10^{-1.87}$), the high-$z$ metallicity drops below $0.1\,Z_\odot$ at $R > 0.5R_{200}$. The median (the

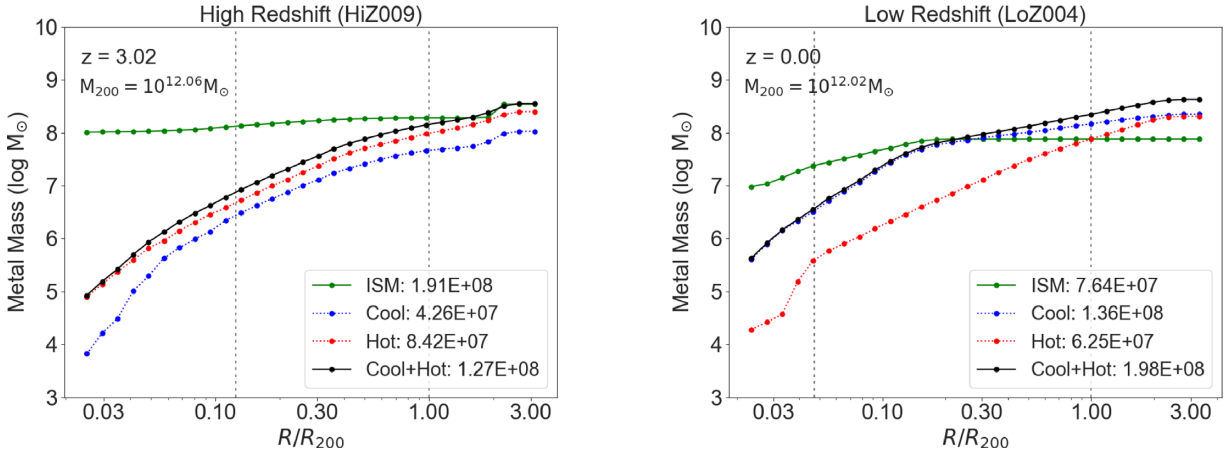

Figure 5. The cumulative gas metal mass plotted as in Fig. 3 for the same two haloes, also shown in Fig. 2. Legends show mass of metals out to R_{200}. At high z, nearly all metals are in the ISM out to R_{200}. At low z, ISM metals dominate only out to $\approx 0.2R_{200}$, where cool metals overtake them. The metal content in the CGM is predominately hot ($T \geq 10^5$ K) at higher redshift and predominately cool ($T < 10^5$ K) at low redshift.

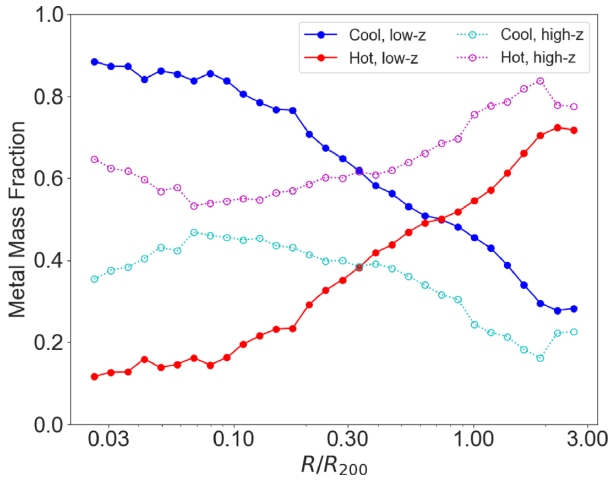

Figure 6. Differential CGM metal fractions divided between cool ($T < 10^5$ K) and hot ($T \geq 10^5$ K) gas as in Fig. 4. Cool metals dominate at $<0.5R_{200}$ at low z, and hot metals dominate beyond R_{200} to at least $3R_{200}$. At high z, CGM metals are mostly found in the hot phase throughout the CGM and into the IGM.

dashed lines in right-hand panels) is comparatively much lower at high z, with at least half the gas remaining at $Z < 10^{-5}$ at $>0.6R_{200}$. Hence, most of the outer cool CGM has $Z \lesssim 10^{-3}$ Z$_\odot$, indicating a primordial origin for much of the extended cool CGM.

The hot phase demonstrates a remarkable contrast to the cool metal evolution, with average metallicities being slightly lower at low z than at high z between 0.15 and $1.5R_{200}$. This extended profile of hot metals is indicative of outflowing thermal winds that are steadily enriching the CGM at high z as we explore in Section 3.3. The low-z inner hot metals approach Z$_\odot$, and their high median and comparatively small dispersions (the dotted lines, right-hand panels) indicate widespread enrichment in the interior $0.1R_{200}$. Extended low-z haloes have a greater dispersion of metals than at high z (cf. the dotted lines at $0.3R_{200}$), suggesting that much of this gas has accreted relatively pristinely and shock heated to the virial temperature.

Many of our general trends match those of van de Voort & Schaye (2012), who explored radial profiles in a variety of haloes in $z = 2$ and $z = 0$ OWLS simulation outputs (Schaye et al. 2010), including stacks of $\approx 10^{12}$M$_\odot$ haloes. Both studies find cool metals in greater abundances at low z than at high z throughout the CGM. In contrast, however, the OWLS simulations show very similar high-z metal abundances between the phases until $0.5R_{200}$, where our simulations show a substantial separation of abundance throughout. It is crucial to note, however, that van de Voort & Schaye (2012) used smoothed particle metallicities (Wiersma et al. 2009b), which spreads metals over the SPH kernel and results in a greater mixing of metals between phases. The main EAGLE simulations (Schaye et al. 2015) also use smoothed metallicities, but our implementation of NEQ ionization and cooling uses discrete, unsmoothed metallicities tied to individual SPH particles, which result in less mixing between phases.

3.3 Velocity

We now discuss velocities, first dividing them into radial and tangential components. The net radial velocity is defined as

$$v_{\rm rad} = \frac{\boldsymbol{v} \cdot \boldsymbol{R}}{R}, \quad (1)$$

where $\boldsymbol{v}$ and $\boldsymbol{R}$ are the velocity and the radial position vectors relative to the central galaxy. Fig. 8 plots the medians of cool and hot gas in the high-z and low-z haloes in the left-hand and right-hand panels, respectively. The dark shading shows the 25–75 per cent (interquartile) range, and light shading shows the 10-90 per cent range. At high z, most cool gas is inflowing while most hot gas is outflowing. Horizontal dashed lines show the typical virial velocity $v_{200} \equiv \sqrt{GM_{200}/R_{200}}$, which is 220 km s^{-1}. Most cool gas inflows slower than $|v_{200}|$, which represents the approximate gravitational speed limit of infalling gas. Hot gas is typically outflowing at high z, with at least 25 per cent of the gas with $v > v_{200}$ at $R < 0.5R_{200}$. This indicates that much of the hot gas at high z is associated with superwind outflows driven by the thermal stellar and AGN superwind prescriptions in EAGLE. It is not clear if hot outflows above v_{200} escape the halo, but positive net velocities are seen out to $1.5R_{200}$ at high z in stark contrast to the cool gas, which is dominated by inflows in the outer halo and beyond.

At low z, the velocities are much smaller when considering absolute values and even less so with relative virial values, where the typical $v_{200} = 146$ km s^{-1}. There is a net inflow of cool gas, but at lower fractional virial values. Hot gas shows a net outflow in the interior 30 kpc, but very rarely is there gas moving in excess of v_{200}.

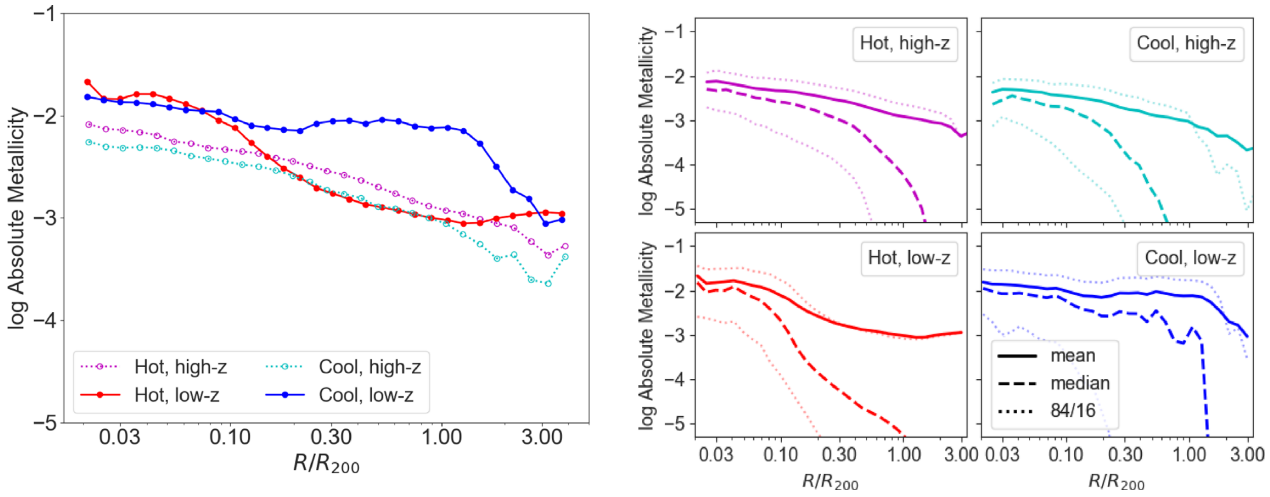

Figure 7. *Left:* Mean absolute metallicities at low and high redshift, split into hot ($T \geq 10^5$ K) and cool ($T < 10^5$ K) gas shown in the solid lines. *Right:* Individual profiles including the dashed lines showing medians and the dotted lines showing 16th and 84th percentiles. Cool gas becomes more enriched by low z, and hot gas has similar metallicities in the outer CGM. The much lower medians for extended high-z cool gas indicate more pristine cool gas in contrast to low-z.

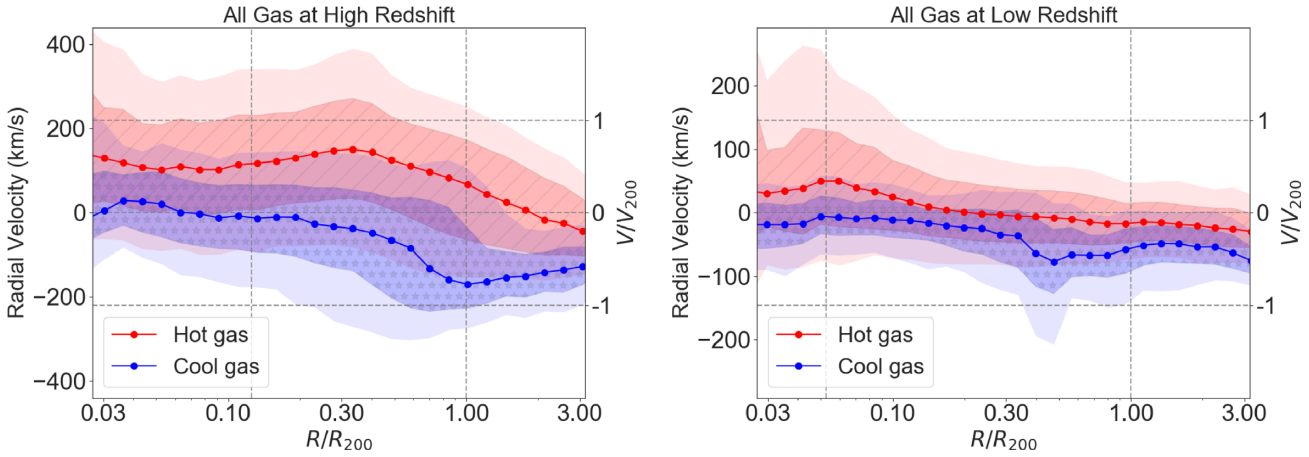

Figure 8. Radial velocity medians (lines) across high-z (right) and low-z (left) halo samples divided into hot ($T \geq 10^5$ K; red) and cool ($T < 10^5$ K; blue) gas. Interquartile (25–75 per cent) ranges in the striped and starred shading, and 10–90 per cent spreads shown in the lighter, solid shading. The horizontal dashed lines represent $v = \pm v_{200}$, and 0 km s^{-1} (left axis scale), and the vertical dashed lines represent 10 kpc and R_{200}. Hot gas velocities at high z indicate strong outflows. High-z cool gas shows net accretion. Velocities are significantly lower at low z, and hot gas transitions from weak outflow to slight inflow at larger radii.

We compare our haloes to those of van de Voort & Schaye (2012), who plotted cool and hot radial velocities from OWLS (Schaye et al. 2010) simulations that used a kinetic wind prescription for stellar feedback (and no AGN feedback scheme). At $z = 2$, their resulting $v_{\rm rad}$ profile shows similar trends as us at $M_{200} \sim 10^{12}$M$_\odot$. Hot gas outflows far beyond the virial radius, then reverses to primarily inflows at $2-3R_{200}$, the same trend we see. Their hot gas achieves a maximum velocity in excess of 100 km s^{-1} at $\sim 0.3R_{200}$. However, by low redshift we find higher $v_{\rm rad}$ for hot gas than van de Voort & Schaye (2012), indicating hot outflows are more prevalent in the EAGLE thermal wind prescriptions for stellar and AGN feedback.

Cold gas flows inwards throughout the entire halo, but reaches a maximum median inflow velocity at $0.8R_{200}$ at high z and $0.5R_{200}$ at low z. The same feature is seen in Kereš et al. (2005; their fig. 19) and van de Voort & Schaye (2012), which indicates cold accretion decelerating due to weak shocks that do not heat the gas into the hot phase. The fact that we see the same trends as the simulations without feedback in Kereš et al. (2005) suggests cool accretion operates in a similar fashion despite the presence of feedback.

In the top panels of Fig. 9, we show the net tangential velocities, defined as the magnitude of the velocity cross-product with radius

$$v_{\rm tan} = \frac{\|\boldsymbol{v} \times \boldsymbol{R}\|}{R}. \quad (2)$$

We also show the co-rotation fraction of the tangential motions (bottom panels), by calculating the fraction of gas particles positively co-rotating with the stellar disc, given by the angular momentum vector of the stars within 30 kpc. There is no preferred direction of rotation if $f_{\rm co\text{-}rotate} = 0.5$. There appears to be a slight preference for co-rotation at high-z (left-hand panel), but much less in the interior compared to low-z. This may stem from the high-z galaxies not having as much organized CGM structure. High-z cool gas at $>0.3R_{200}$ has slightly greater tangential motion than both high-z hot

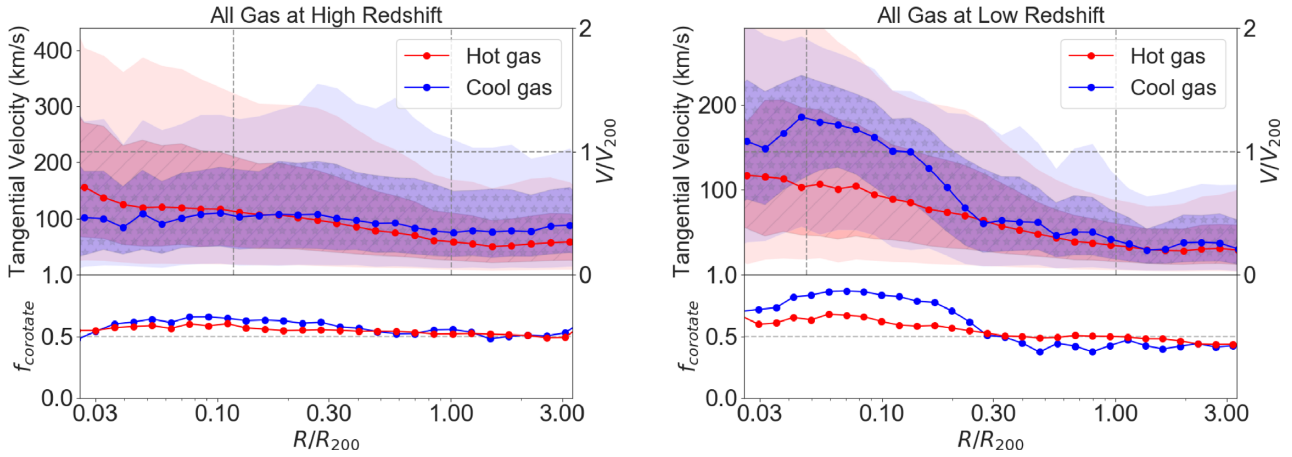

Figure 9. Tangential velocities plotted as in Fig. 8. Top panels show the magnitude of tangential velocities. Bottom panels show the fraction of tangential gas particles co-rotating with the stellar disc ($f_{\rm corotate} = 0.5$ indicates no preferred direction). Low-z cool ($T < 10^5$ K) gas indicates significant rotation in the inner $0.2R_{200}$, consistent with disc-like structures extending into the CGM. Low-z hot ($T \geq 10^5$ K) gas shows sub-virial co-rotation.

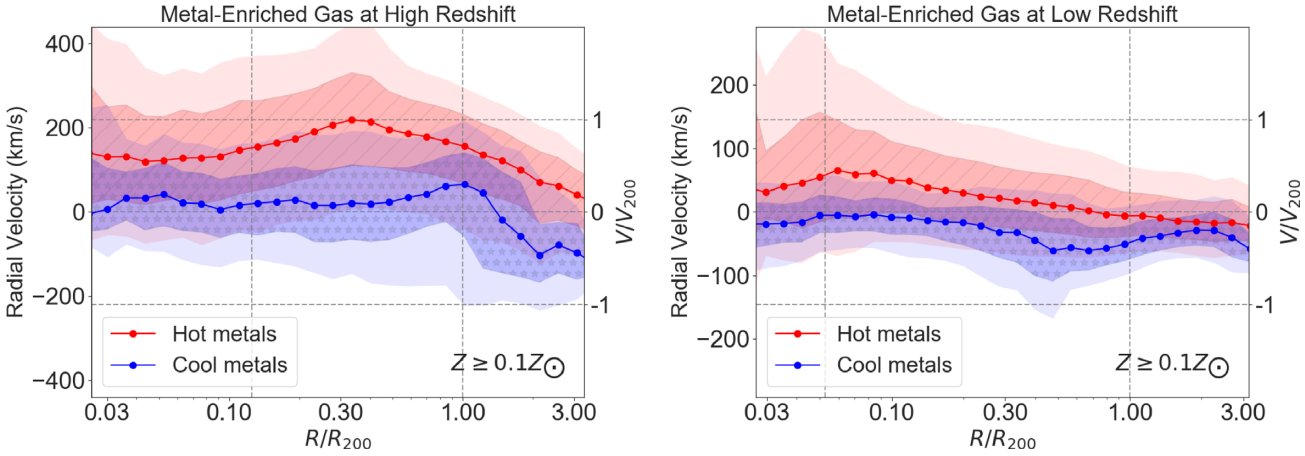

Figure 10. Radial velocities of metal-enriched gas ($Z \geq 0.1\,{\rm Z}_\odot$) as plotted in Fig. 8. Medians are shown as the points, interquartile (25–75 per cent) ranges in the striped and starred shading, and 10–90 per cent spreads in the lighter, solid shading. Hot metals at high z are strongly outflowing and show weaker outflows at low z. Cool ($T < 10^5$ K) metals are preferentially flowing outwards at high z and inwards at low z.

gas and low-z cool gas as indicated by a higher median $v_{\rm tan}$ and a broader dispersion. This could be an indication of cool, pristine accretion transporting angular momentum to the galaxy (e.g. Stewart et al. 2011).

By $z = 0$ (right-hand panel), cool tangential velocities approach and exceed the virial velocity in the inner CGM and exhibit high co-rotation fractions. This indicates the cool gas is organized into primarily rotationally supported discs extending out to $R \approx 40$ kpc in our simulations. Present-day hot haloes also show higher tangential velocities than their high-z counterparts, and the tangential motion inside $0.3R_{200}$ indicates co-rotation with the galaxy's preferred axis. Oppenheimer (2018) showed that these same low-z haloes deviate significantly from hydrostatic equilibrium (HSE) owing primarily to significant tangential support of the inner hot halo, which in part exhibit sub-centrifugal rotation but also have uncorrelated tangential motions. In contrast, the high-z haloes do not show evidence for such tangential support in their hot haloes. The high-z CGM does not show indications of dynamical stability, which contrasts with low-z hot haloes at $r \gtrsim 50$ kpc that are mainly supported by a thermal pressure gradient (Oppenheimer 2018).

Tangential velocities were also explored using the Illustris-TNG simulations by DeFelippis et al. (2020), where they also found higher cool than hot $v_{\rm tan}$ that greatly increase inside $0.5R_{200}$ for $z = 0$ $10^{11.75-12.25}{\rm M}_\odot$ haloes. They divide their sample into quartiles based on specific stellar angular momentum, j_*, and examine all L^* centrals in Illustris-TNG, while excising gas bound to satellites. Our low-z haloes preferentially host spiral galaxies, which suggest they have higher j_* than the typical L^* central. However, our galaxies are unlikely to all be within the highest quartile of j_* in the EAGLE volume, which is the quartile for which DeFelippis et al. (2020) finds the greatest tangential velocities.

In Figs 10 and 11, we present the radial and tangential velocities but including only metal-enriched gas, which in this case are gas particles with $\geq 0.1\,{\rm Z}_\odot$ metallicity. At high z, the hot metals show slightly faster moving outflows, reaching a median of 200 km s^{-1} near $0.3R_{200}$, as shown in Fig. 10 (left-hand panel). This indicates that metals are preferentially being transported to a large fraction of the halo radius, often becoming ejected from high-z haloes. The flow of cool metals is also different from that of the total cool gas with median outflows near 0 km s^{-1} and even positive approaching R_{200}. This result contrasts with the cool gas in Fig. 8 that indicates

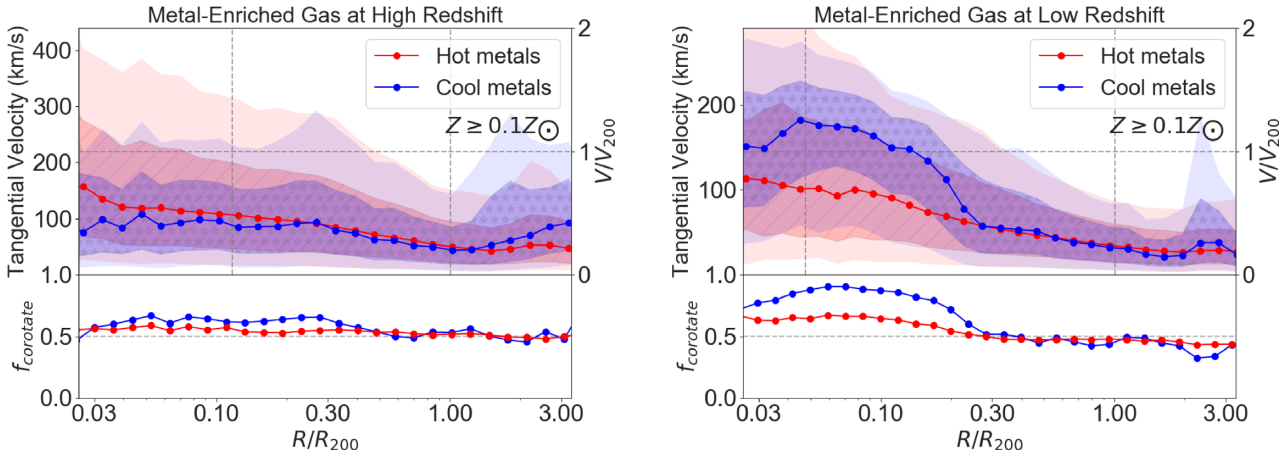

Figure 11. Tangential velocity magnitudes and co-rotation fractions of metal-enriched gas ($Z \geq 0.1\,Z_\odot$) as plotted in Fig. 9. Medians are shown as the points, interquartile (25–75 per cent) ranges in striped and starred shading, and 10–90 per cent spreads in the lighter, solid shading. Metals show similar medians as gas. At high z, tangential spreads are less for the metals, which are preferentially outflowing. At low z, spreads are similar to gas, indicating that metals are well mixed.

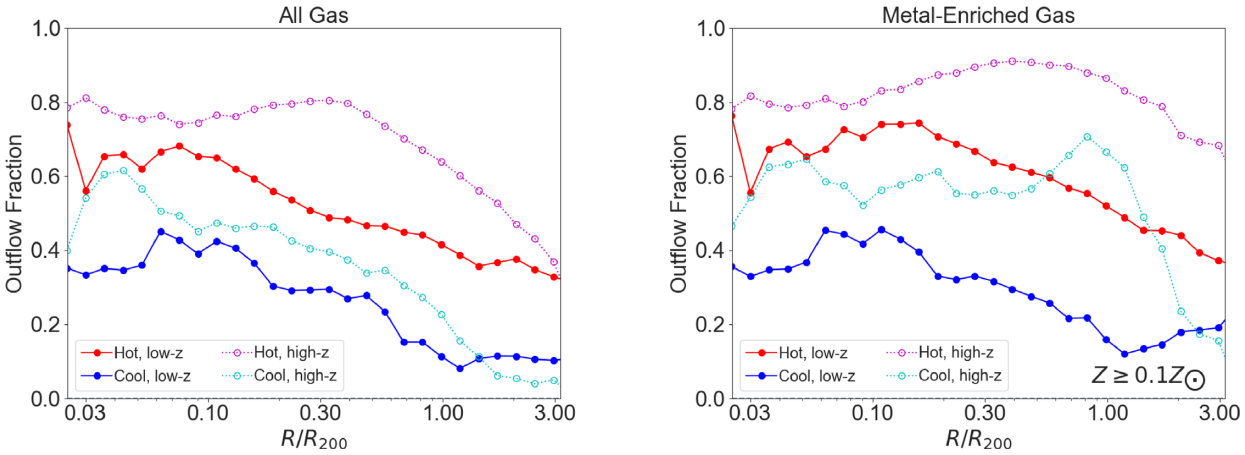

Figure 12. Outflowing fraction of all gas (left) and metal-enriched gas ($Z \geq 0.1\,Z_\odot$; right) of all high-z (dotted) and low-z (solid) haloes. Hot gas ($T \geq 10^5$ K) is more dominated by outflows than cool gas ($T < 10^5$ K), as is high-metallicity gas relative to all gas. Cool high-z gas is generally inflowing, but the metals indicate more outflows.

primarily inflowing gas. We predict UV absorption kinematics of cool gas (e.g. H I) and cool metals (e.g. C II, Si III, Mg II) to be different at high z.

By low redshift, the radial velocity profiles between high-metallicity gas (Fig. 10, right-hand panel), and all gas (Fig. 8, right) exhibit similar shapes and trends. One difference is that the hot metals are outflowing at higher velocities than the corresponding hot gas, with a net outflow continuing all the way to $0.7R_{200}$, whereas the hot gas only shows a net outflow to $0.2R_{200}$.

Turner et al. (2017) also explores radial velocities at $z \approx 2$ using the main EAGLE volume, finding net inflows for gas, H I, and even metal species (C IV, Si IV) from beyond 1 Mpc to at least 70 kpc in their fig. 8. Our high-z zooms suggest more of a net outflow in the outer CGM where our plot overlaps theirs, but this heavily depends on the cut applied to metals. If a $Z \geq Z_\odot$ cut is used instead for Fig. 5, strong radial outflows extend beyond R_{200}. Lower metallicity thresholds result in greater inflows, hence the Turner et al. (2017) result suggests metal ions arise primarily from lower metallicity gas, although there are differences in simulation resolution and halo selection.

Moving on to tangential velocities of the metals in Fig. 11, both cool and hot metals show similar profiles at high z (left-hand panel), but cool metals exhibit less overall tangential motion than the gas (cf. Fig. 9). This indicates that metals are on a preferentially radially outflowing trajectory at high z. By low z (right-hand panel), the tangential profiles of cool and hot metals are essentially statistically indistinguishable from gas, indicating that metals are well mixed throughout the CGM and exhibit specific angular momentum profiles that are similar to gas (see Section 3.4).

Finally, we sum up the results of mass and metals by showing the outflow fraction in Fig. 12, where we plot the fraction of gas with net positive radial velocity across our four main subdivisions (high z/low z and hot/cool) for all gas (left-hand panel) and high-metallicity gas (right-hand panel). In general, hot gas is more outflowing than cool gas, particularly at high z. Cool gas has a similar inflowing proportion at both epochs. Metal-enriched gas has comparatively more outflows in all cases. The most obvious divergence in trends is that cool, high-z metal-enriched indicates more outflows in contrast with its primarily inflowing nature at low z. Cool gas probed by UV absorption lines

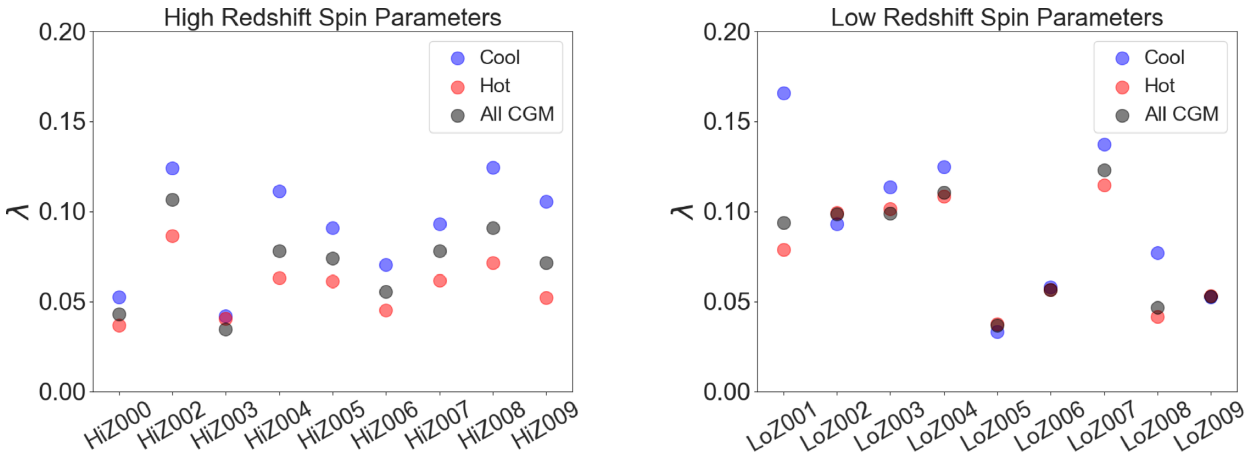

Figure 13. Angular momentum spin parameters of the nine high-z (left) and nine low-z haloes (right). All CGM gas is plotted as the black points, cool ($T < 10^5$ K) gas as the blue points, and hot ($T \geq 10^5$ K) gas as the red points. Hot gas always has lower spin parameters than cool gas at high z, and spin parameters have higher averages at low z. Given that most of the CGM mass is hot at low z, there is more angular momentum in the hot phase than the cool phase.

may exhibit larger absolute velocities at high z than low z, which could be a signature of outflows.

Hafen et al. (2019) analysed FIRE-2 simulations focusing on the origin of the CGM at $z = 0.25$ and $z = 2$ via particle tracking of individual gas elements. Their $\sim 10^{12}$M$_\odot$ haloes exhibit many of the trends we see here, including winds from the central galaxy extending much further into the CGM at $z = 2$ than at $z = 0.25$. Their use of tracking finds that much more of the $z = 2$ CGM gas originates from central galaxy winds than at $z = 0.25$, where the dominant origin of CGM gas is accretion from the IGM (their fig. 9). Like our haloes, their $\sim 10^{12}$M$_\odot$ haloes at low z are dominated by hot gas while their highest mass $z = 2$ haloes ($\sim 10^{11.7}$ M$_\odot$) show more of an equitable split between cool and hot phases (their fig. A1). Our lower velocities at low-z indicate that gas cycles through the CGM significantly more slowly than at high-z, which agrees with the Hafen et al. (2020) finding that half of the FIRE-2 low-z CGM remains within the virial radius as CGM gas for $\sim$3 Gyr, while most of the $z = 2$ CGM gas will either accrete on to the galaxy or be ejected from the halo within a Gyr (their figs 2 and 5). The vast majority of their $z = 0.25$ CGM gas that remains in the CGM is hot, while the cool CGM more likely accretes on to the central or a satellite (their fig. 6) and Hafen et al. (2019) finds the cool gas is more aligned along the disc of the galaxy as opposed to a more spherical distribution of the hot gas. Our haloes retain fewer baryons overall inside the virial radius than FIRE-2, which have higher low-z stellar fractions (Hafen et al. 2019, their fig. 1) suggesting that our CGM gas is less likely to be accreted on to the central galaxy and more likely to be ejected from the CGM. This in part owes to the presence of AGN feedback in our simulations, which is absent in the FIRE-2 simulations.

3.4 Angular momentum

The angular momentum of the CGM has significant implications for the gas that accretes on to a galaxy, forms stars, and builds a galaxy's morphology. In our selection of star-forming galaxies at high and low z, we derive halo spin parameters:

$$\lambda = \frac{j}{\sqrt{2} R_{200} v_{200}}, \tag{3}$$

where the specific angular momentum j is defined as

$$j = \frac{\|\boldsymbol{J}\|}{\sum_i m_i}, \tag{4}$$

and $\boldsymbol{J}$ is the angular momentum vector sum:

$$\boldsymbol{J} = \sum_i m_i \boldsymbol{v}_i \times \boldsymbol{R}_i, \tag{5}$$

over particle indices i. In Fig. 13, we plot the halo spin parameters for both high and low z. In both samples, the cool phase of the CGM tends to have more angular momentum than the hot phase. The median total CGM spin parameters and interquartile spreads are $\lambda = 0.074^{+0.004}_{-0.019}$ ($0.094^{+0.005}_{-0.041}$) at high (low) z. A notable difference is the decline in the spread of angular momenta between cool and hot gas at later times. At high z, the median $\lambda_{\rm hot}$ is 0.061, which is 65 per cent of the median $\lambda_{\rm cool} = 0.093$. By low z, the difference is less with $\lambda_{\rm hot} = 0.079$, which is 85 per cent of $\lambda_{\rm cool} = 0.093$. The $\lambda_{\rm cool}$ values are well within the range of previous studies that show $\lambda_{\rm cool}$ to be several times that of the dark matter, $\lambda_{\rm DM}$ (Stewart et al. 2011, 2017). Stevens et al. (2017) showed that EAGLE haloes in general have higher $\lambda_{\rm hot}$ than $\lambda_{\rm DM}$, and Oppenheimer (2018) showed that these low-z haloes had $\lambda_{\rm hot} = 3 \times \lambda_{\rm DM}$.

The low-z combination of the total mass of the CGM being dominated by the hot phase and $\lambda_{\rm hot}$ being a high fraction of $\lambda_{\rm cool}$, means that the median angular momentum of the hot halo out to R_{200} is about 5 × that of the cool CGM, with values of $\boldsymbol{J}_{\rm hot} = 2.4 \times 10^{14}$ and $\boldsymbol{J}_{\rm cool} = 4.7 \times 10^{13}$ M$_\odot$ km s^{-1} kpc, respectively. The low-z hot CGM is the largest repository of angular momentum of any phase. Most of the hot angular momentum is spatially extended with < 10 per cent of the $\boldsymbol{J}_{\rm hot}$ coming from $<0.3R_{200}$, which contrasts with $\boldsymbol{J}_{\rm cool}$ for which the proportion from $<0.3R_{200}$ is half. At high z, the cool CGM has total angular momentum 75 per cent higher than the hot CGM (cf. $\boldsymbol{J}_{\rm cool} = 8.1 \times 10^{13}$ versus $\boldsymbol{J}_{\rm hot} = 6.0 \times 10^{13}$ M$_\odot$ km s^{-1} kpc), in large part due to the hot CGM being primarily outflowing and not rotating. If the ISM criterion uses only SFR > 0, instead of our definition described in Section 2.3, then $\boldsymbol{J}_{\rm cool}$ becomes 1.0×10^{14} M$_\odot$ km s^{-1} kpc at high z but negligible difference at low z.

We also consider angular separation θ in degrees between the angular momentum vectors of the cool CGM, hot CGM, and the stellar component in Fig. 14. The cool and hot CGM are fairly well

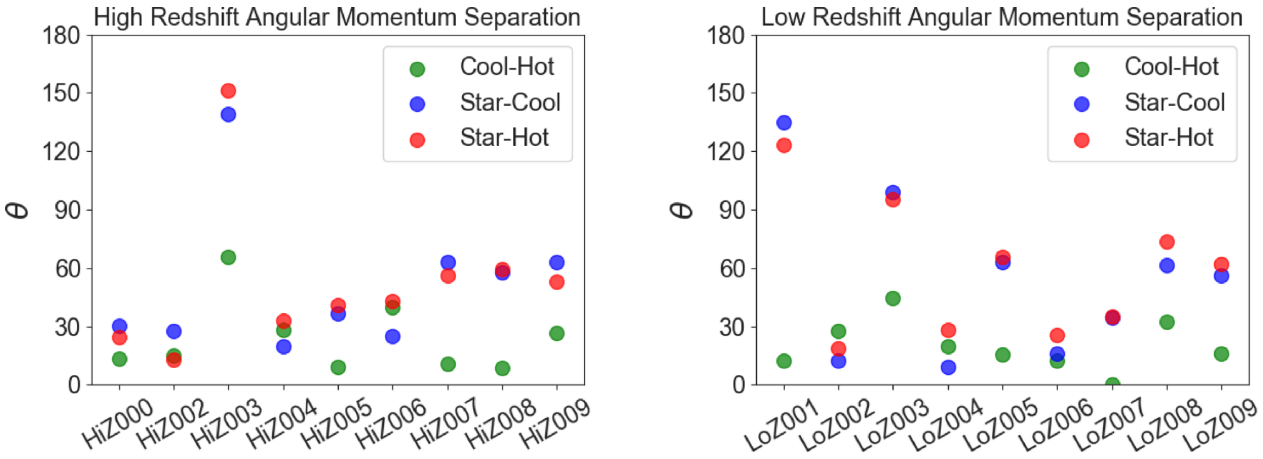

Figure 14. The angles of separation between the hot ($T \geq 10^5$ K) and cold ($T < 10^5$ K) gas angular momentum vectors (Cool–hot) are plotted as the green points. The angle between the cool (hot) CGM angular momentum vectors and the stellar angular momentum vectors are plotted as the blue (red) points. Haloes at high and low z exhibit well-aligned angular momentum for their hot and cool CGM, but significant mis-alignment between the angular momenta of the CGM and stellar disc is typical at both high and low z. Low-z galaxies with all vectors well aligned often have grand design spiral morphologies, including halo LoZ004 shown in the right-hand panel of Fig. 2.

aligned with a median angle of $\theta_{\text{cool–hot}} = 15^\circ$ (16°) at high (low) z. However, the alignment is less between the stellar component (all stars within 30 physical kpc) and the CGM with median $\theta_{\text{star-cool}} = 37^\circ$ (56°) and $\theta_{\text{star-hot}} = 43^\circ$ (62°).

Stevens et al. (2017, their fig. 14) also looked at angles between cool and hot gas, finding a somewhat greater offset between the cool and hot CGM than our haloes, though this may be in part due to their differing definition for 'cold' gas, where they include ISM, plus our selection of only star-forming galaxies. Nevertheless, there is strong alignment between the cool and hot CGM, and more randomness with the orientation of the stellar disc, which represents the integrated result of accretion and star formation over all previous epochs. We check that the greater star-cool angles do not contradict the cool CGM rotating disc-like structure aligned with the stellar component at low z in Fig. 9 that show strong co-rotation between the stellar and inner ($\lesssim 0.2R_{200}$) cool CGM. Mis-alignment often arises from extended cool CGM structures with significant angular momentum at large radii and no correlation with the stellar disc. On the other hand, some of the most well-aligned galaxies along all three vectors in Fig. 14 (e.g. LoZ002, LoZ004, LoZ007) appear as grand design spirals with extended CGM discs (cf. Fig. 2, right-hand panels).

DeFelippis et al. (2020) find stronger alignment between the stellar and CGM angular momenta in their highest j_* quartile with $\theta_{\text{star-cool}} \approx 15^\circ$ and $\theta_{\text{star-hot}} \approx 27^\circ$ in Illustris-TNG (their fig. 2). Their lowest j_* quartile shows angles of $\approx 60^\circ$, more similar to our results. The existence of extended CGM structures, including the CGM associated with satellites that is excised by DeFelippis et al. (2020), likely biases high our angles between stars and the CGM. We therefore analyse the angular momentum alignment in our haloes after filtering out the CGM around satellites with the goal of assessing the impact of these extended CGM structures. At high (low) z, we filter out CGM gas within 10 (20) physical kpc of any subhalo that has a stellar mass $>10^5$ M$_\odot$ (essentially any star particle given our resolution). We find that the cool and hot CGM have a median angle of $\theta_{\text{cool–hot}} = 13^\circ$ (14°) at high (low) z. The stellar component and the CGM have a median of $\theta_{\text{star-cool}} = 41^\circ$ (54°) and $\theta_{\text{star-hot}} = 47^\circ$ (56°). The decrease in separation by several degrees at low-z of all three vector pairs suggests that CGM of satellites only contribute slightly to angular momentum misalignment in our gaseous haloes. However, like us, DeFelippis et al. (2020) find that the hot specific angular momentum, j_{hot}, is a significant fraction of the j_{cool} at both $z = 0$ and $z = 2$.

3.5 Hot gas radial profiles

The hot gas dominates the CGM volume around L^* galaxies (e.g. Bregman 2007; Stocke et al. 2013) therefore we plot volume-weighted radial profiles of this component in Fig. 15. The gas density (upper left-hand panel) shows flatter radial profiles at low z than at high z with the following fits to the medians of the nine haloes between $R = 0.1$ and $1.0R_{200}$, using

$$n_{\text{H}} = n_{\text{H},R_{200}} \left(\frac{R}{R_{200}} \right)^{-\alpha_{n_{\text{H}}}}, \tag{6}$$

where $\alpha_{n_{\text{H}}} = 1.6$ at high z and becomes 1.1 at low z. $n_{\text{H},R_{200}} = 9.0 \times 10^{-5}$ and 1.4×10^{-5}cm^{-3} at the two respective redshifts. The temperature profiles flatten towards the centre, and decline with power laws fit between 0.1 and $1.0R_{200}$ using

$$T = T_{R_{200}} \left(\frac{R}{R_{200}} \right)^{-\alpha_T}. \tag{7}$$

At high (low) z, $T_{R_{200}} = 1.1 \times 10^6$ (2.2×10^5) K and $\alpha_T = 0.5$ (0.8).

We also plot the entropy profiles

$$K = T n_e^{-2/3} \tag{8}$$

in the lower left-hand panel of Fig. 15, where n_{e} is the free electron density. At high z, entropy is rising with R, and slightly flattening at large R. This gas is strongly outflowing (Fig. 8), which may indicate high-entropy gas is preferentially traversing outward resulting in this profile. Entropy-driven winds (Bower et al. 2017; Keller, Kruijssen & Wadsley 2020) appear to play an essential role in ejecting gas from high-z haloes that exhibit higher outflow rates through the virial radius than their low-z counterparts in EAGLE (Mitchell, Schaye & Bower 2020b, their fig. 1). At low z, entropy rises only in the inner $0.1R_{200}$, where it also coincides with positive radial outflows in Fig. 8 that are much weaker than at high z. Beyond, the entropy actually falls slightly before it recovers in the outer halo. This coincides with

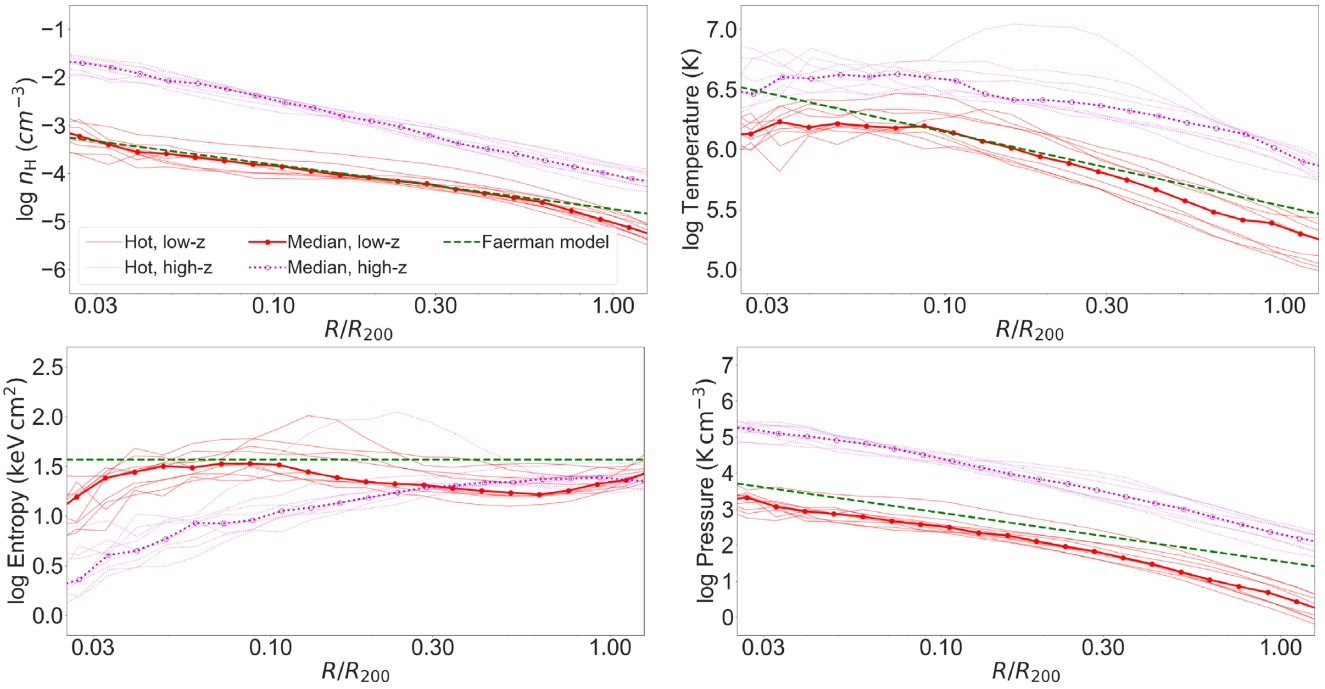

Figure 15. Volume-weighted radial trends of the density, temperature, entropy, and pressure for hot phase gas at high z (dotted magenta) and low z (solid red). Stacked medians of the profiles are shown with the thicker lines. The Faerman, Sternberg & McKee (2020) isentropic model is shown in dashed green for a $z = 0$ Milky Way-like hot halo.

median hot $v_{\rm rad} \approx 0$ km s^{-1}, which indicates a different source of the outer hot halo. Much of this gas has very low metallicity (Fig. 7), which suggests a source of accretion from the IGM. It is curious that rising entropy profiles often coincide with outflowing gas at both both epochs because such entropy profiles are also indicative of dynamically stable configurations in the centres of clusters, although such profiles are typically steeper (e.g. Voit, Kay & Bryan 2005).

Finally, we plot pressure profiles,

$$P = n_{\rm H} T, \tag{9}$$

in the lower right-hand panel, where high-z pressures are higher everywhere than at low z. The pressure at fixed M_{200} should scale approximately as R_{200}^{-4}, which gives the ≈30−40 factor in pressure difference between low and high z. This appears to be the case at $R = 0.2R_{200}$, but the difference is greater at lower (higher) radii where high-z haloes are denser (hotter) than self-similar scaling relations.

We overplot the green-dashed lines in Fig. 15 of the Faerman et al. (2020) $z = 0$ isentropic hot halo profiles in all panels. Their model, developed for a Milky Way-like halo, is a reasonable representation of our flat low-z entropy profile between 0.1 and $1.0R_{200}$. Our densities and temperatures also show good agreement, especially in the inner halo. Our pressure profile is lower than the Faerman et al. (2020) model that also includes non-thermal sources of turbulent and magnetic/cosmic ray pressure. That model assumes HSE, but Oppenheimer (2018) showed that these low-z haloes are not well described by HSE in their inner CGMs, though at $\gtrsim 0.5R_{200}$ the thermal pressure gradient accounts for ≥ 75 per cent of the support against gravity (their fig. 2).

We also contrast to the Stern et al. (2019) hot gas steady-state cooling flow models for Milky Way-mass haloes, which have more steeply rising entropy profiles as a result of higher $\alpha_{n_{\rm H}}$ and lower α_T. Resolving X-ray profiles around Milky Way-like galaxies (e.g. Li & Wang 2013) as has been done for more massive spirals (Anderson, Churazov & Bregman 2016; Bogdán et al. 2017; Li et al. 2017; Das et al. 2019) can help distinguish these contrasting models. Central X-ray emission from individual galaxies may be detectable with the *Chandra* X-ray telescope according to Illustris-TNG simulations (Truong et al. 2020) and the *eROSITA* mission should be able to observe extended emission in stacks of haloes as predicted by both the EAGLE and Illustris-TNG simulations (Oppenheimer et al. 2020b).

4 DISCUSSION

4.1 CGM mass contents

In Table 1, we list $f_{\rm CGM} \equiv M_{\rm CGM}/M_{200}(\Omega_{\rm M}/\Omega_{\rm b})$, the total mass content of the CGM (here defined as inside R_{200}) normalized to the cosmic baryon fraction. $f_{\rm CGM}$ averages 0.34 at high z and is 0.47 at low z. At high z, Pezzulli & Cantalupo (2019) calculated that $f_{\rm CGM} \geq 0.70$ across cool and hot phases are necessary to reconcile giant Lyα emission nebulae observed around quasar hosts, which they assume live in haloes of $M_{200} \sim 10^{12}$ M$_\odot$. However, this higher value than our $f_{\rm CGM}$ can be rectified if these quasar hosts have higher halo masses, which both lowers the $f_{\rm CGM}$ that Pezzulli & Cantalupo (2019) calculate in their analysis and raises the $f_{\rm CGM}$ using higher halo masses in EAGLE that generally have higher $f_{\rm CGM}$ (Davies et al. 2019).

The low-z average $f_{\rm CGM}$ value is significantly higher than the typical value observed at similar halo mass in the EAGLE Ref-L100N1504 volume with 8 × lower mass resolution, where the average $f_{\rm CGM} = 0.22$ for haloes with $M_{200} = 10^{11.75-12.25}$ (Davies et al. 2020). However, the EAGLE Recal-L025N0752 volume, from which the low-z haloes are selected and that has the same resolution, shows a higher average $f_{\rm CGM} = 0.35$ (J. Davies, private communication). Our low-z sample $f_{\rm CGM}$, which averages 0.47, is 34 per cent higher

than the average $f_{\rm CGM}$ for all haloes of the given mass range in the volume. Our sample's $f_{\rm CGM}$ being biased high is to be expected given that our haloes host star-forming galaxies, which Davies et al. (2019) and Oppenheimer et al. (2020a) demonstrated have higher baryon fractions owing to stellar and black hole feedback preferentially ejecting CGM gas from haloes hosting passive galaxies (see also Terrazas et al. 2020; Davies et al. 2020, for discussion of this effect in the Illustris-TNG simulation). Oppenheimer et al. (2020a) found a similar difference in the Ref-L100N1504 volume, where the highest quartile of sSFR for $M_{200} = 10^{12.0-12.3}{\rm M}_\odot$ haloes have $f_{\rm CGM}$ values 30 per cent higher than the mean $f_{\rm CGM}$ for all haloes. Hence, our star-forming sample appears to be less affected by the phenomenon of black hole feedback ejecting baryons than the typical halo in our mass range.

4.2 CGM metal contents

Peeples et al. (2014) calculated the expected metal content yielded from stars over cosmic history, finding that the stellar and ISM contributions fell far short of the expected metal content, by at minimum a factor of 2. Our 'LoZ' simulations confronted this shortfall in O16, arguing that most metals are ejected into the CGM and IGM, often beyond R_{200}. Our average CGM metal contents at $z = 0$ are 1.6×10^8 M$_\odot$ for cool metals and 1.2×10^8 M$_\odot$ for hot metals, which are both more than the ISM metal content, 1.1×10^8 M$_\odot$. The content of metals recycled into later generations of stars is 3.3×10^8 M$_\odot$. O16 quantified the oxygen content ejected beyond R_{200} at $\approx 35-40$ per cent of the expected oxygen yield for $10^{12}{\rm M}_\odot$ haloes, hence we expect $3-5 \times 10^8$ M$_\odot$ more diffuse metals beyond R_{200} given the yields and nucleosynthetic sources of metals used in EAGLE.

Hafen et al. (2019) found a much greater fraction of the metal yield ends up in stars at $z = 0.25$ in FIRE-2 (70–90 per cent, their fig. 3) than in our haloes (25–35 per cent at $z = 0.2$, O16, their fig. 9). Oppenheimer et al. (2018b, their section 5.1) discussed that EAGLE–CGM simulations have yields that are consistent with Peeples et al. (2014) but are higher than the ones used in FIRE-1 (Muratov et al. 2017), where stellar metallicites are similar to O16 but CGM metallicities are much lower. Hafen et al. (2019) discussed in their section 4.1.2 that FIRE-2 has similar metal yields as FIRE-1, which are about half as much as used by Peeples et al. (2014). Our simulations yield more metals and place proportionally more of those metals in diffuse gas, resulting in higher CGM metallicities (Fig. 7) than FIRE-2 (Hafen et al. 2019, their fig. 18). Oppenheimer et al. (2018b) found that their higher metallicities are necessary to reproduce COS–Haloes low-ion metal absorber statistics (Werk et al. 2013), but given the uncertainty in ionization corrections it is very possible that fewer metals are necessary to reproduce observed low-ion metal absorbers.

At high z, we find an average of 4.2×10^7, 6.9×10^7, and 2.0×10^8 M$_\odot$ of metals in the cool CGM, hot CGM, and ISM, respectively. This totals to 3.1×10^8 M$_\odot$, which is similar to the amount of metals in stars, 2.8×10^8 M$_\odot$, in these high-z haloes. A smaller fraction of metals is ejected beyond R_{200}, though we save a complete accounting of high-z metals in the context of the missing metals problem at $z = 2-3$ (e.g. Bouché et al. 2007) for further work.

4.3 Are low redshift hot haloes rotating?

We show in Fig. 9 that low-z hot haloes show a net rotation that is aligned with the stellar axis, but substantially sub-centrifugal as the median $v_{\rm tan} \approx 40$ km s^{-1} inside $0.1R_{200}$. Hodges-Kluck, Miller & Bregman (2016) calculated a rotation speed of 183 ± 41 km s^{-1} for the Milky Way's hot halo by measuring O VII absorption line centroids. While this is 75 per cent of the solar rotational speed around the Galactic centre of 240 km s^{-1} (Reid et al. 2014), our low-z simulations do not exhibit as high values for hot halo co-rotation as the Milky Way, and our hot halo rotational axes are often substantially mis-aligned with the stellar disc (Fig. 14). Furthermore, a closer examination of the measured velocities as a function of Galactic latitude and longitude in fig. 5. of Miller, Hodges-Kluck & Bregman (2016) shows significant scatter and deviations from aligned co-rotation, which they argue requires a much higher resolution X-ray spectrometer to accurately observe.

Oppenheimer (2018) found that our low-z inner haloes have significant uncorrelated tangential motions that do not add to the summation of net directional rotation or angular momentum. Nevertheless, this paper did argue that there existed as much angular momentum in the inner hot haloes as calculated by Hodges-Kluck et al. (2016) out to 90 kpc. The low-z galaxies with larger grand design spiral appearances (LoZ002, LoZ004, LoZ007) have among the highest hot halo spin parameters (Fig. 13) and aligned spin axes (Fig. 14). In the future, it would be useful to consider how total angular momentum in the hot CGM relates to galactic morphology.

4.4 Results in context of other EAGLE simulations

We now discuss some recent results from EAGLE that mainly use the lower resolution Ref-L100N1504 volume in the context of our results. Fundamentally, the high-z haloes are growing at nearly an order of magnitude faster than their low-z counterparts. Mitchell et al. (2020a) shows in their fig. 1 that a 10^{12} M$_\odot$ halo doubles its mass in 0.6 Gyr at $z \approx 3$ and 5 Gyr at $z = 0$. They also show that the gaseous content doubles at a lower rate: 1 Gyr at $z \approx 3$ and 15 Gyr at $z = 0$. Feedback drives gas out of haloes (Section 3.3), which likely plays a major role in reducing the rate of the gaseous growth relative to the dark matter growth. Because our higher resolution haloes are not as evacuated and are selected to be star-forming, which have higher $f_{\rm CGM}$ than the average halo at the given mass (Section 4.1), it is likely that our gaseous halo growth rates are faster than Mitchell et al. (2020a) and may be nearer the total halo growth rates.

Mitchell et al. (2020a) calculates mass outflow rates of gas particles leaving the halo in the Ref-L100N1504 volume. Their fig. 11 shows that 10^{12} M$_\odot$ marks the halo mass transition from stellar winds dominating to AGN winds dominating for both high-z and low-z in EAGLE. To distinguish more precisely the role of stellar versus AGN feedback at the Ref-L100N1504 resolution, we obtain the absolute outflow rates with the normal EAGLE prescription and compare them to the No-AGN EAGLE model (P. Mitchell private communication). At $z = 2.5$, the typical outflow rate through R_{200} for $M_{200} = 10^{12}$ M$_\odot$ is 18 M$_\odot$ yr^{-1}, but reduces to 9 M$_\odot$ yr^{-1} without AGN. At low-z, these values are 10 and 7 M$_\odot$ yr^{-1} with and without AGN. Our haloes will likely have lower values for these outflow rates with less impact for AGN given the trends in our sample's $f_{\rm CGM}$ values.

It is useful to consider the findings of Mitchell et al. (2020a) for the morphology of the outflows given our finding of organized CGM disc structure at low-z relative to high-z. They analyse the angular dependence of outflow rates, showing a clear biconical pattern with preferential alignment pointing orthogonal to the discs at $z = 0.25$ in their section 3.6. At high-z, the morphology of these winds is still uncertain and will be the focus of future work.

Finally, we note that galaxy morphology does not change systematically with numerical resolution in EAGLE, which suggests that our primarily star-forming, spiral galaxies should remain morphologically similar at lower resolution. Thob et al. (2019) demonstrated

morphology as measured by stellar kinematical parameters appears converged between the Ref-L100N1504 and Recale-L025N0752 simulations.

5 SUMMARY

We have presented the physical characteristics of circumgalactic haloes simulated at high ($z \approx 2-3$) and low ($z = 0$) redshifts using a set of EAGLE zoom simulations of $10^{12}\,M_\odot$ haloes hosting star-forming galaxies. These simulations demonstrate the changes in the CGM around L^* galaxies at two epochs separated by 10 Gyr. The mean M_{200} of our nine high-z (low-z) haloes is $10^{12.04}$ ($10^{12.07}$) $M_\odot$. The primary results are as follows:

(i) High-z gaseous haloes have nearly as much cool ($T < 10^5$ K) gas as hot ($T \geq 10^5$ K) gas out to R_{200}, while low-z haloes have 5 × more hot gas than cool gas. The low-z CGM phases are more sorted by radius than for haloes at high z, with the cool phase being larger in the inner 50 kpc, and the hot phase dominating at larger radii (Figs 3 and 4).

(ii) The high-z ISM has 1.5 × the total metal content of the high-z CGM, while the low-z CGM has 2.6 × the metal content of the low-z ISM. The high-z hot CGM contains 60 per cent more metals than the cool CGM, while this reverses at low z with the cool CGM having 35 per cent more metals than the hot CGM content (Fig. 5).

(iii) The metals are evenly distributed between the hot and cool phases throughout the high-z CGM. At low z, the cool metals dominate the interior and the hot metals are more prevalent at larger radii. Cool metallicities increase from about $0.1\,Z_\odot$ to $1\,Z_\odot$ from high to low z indicating much of the cool gas is pristine accretion at high z and recycling gas at low z. Hot metals have less scatter and intermediate metallicities that change less across time, which is a signature of their thermal feedback-driven origins using the EAGLE prescription (Figs 6 and 7).

(iv) Hot gas shows substantial outflows at high z, which stands in contrast to the cool gas that is primarily accreting with the highest inflow velocities being in the outer halo where the gas is relatively pristine. Low-z radial velocities are much lower with only inner hot gas showing a net outflow, and cool gas accreting at a much lower rate (Figs 8 and 12).

(v) Hot metal-enriched ($Z \geq 0.1\,Z_\odot$) gas shows larger outflow velocities than all hot gas at both epochs. Cool metals, like all cool gas, are primarily inflowing at low z. High-z cool metals indicate less inflows than all cool gas, and their kinematics show proportionally more outflows when a higher Z threshold is applied. The high-z cool CGM has different origins, which depend sensitively on the baryon or metal tracer used (Figs 10 and 12).

(vi) The cool low-z CGM shows a net positive rotation out to $0.2R_{200}$, indicating disc-like CGM structures extending out 40 kpc around L^* galaxies. Hot gas at low z also shows substantially net positive rotation, but no preferred rotation beyond ≈50 kpc. These low-z hot haloes have been shown to be supported primarily by tangential velocities in the inner CGM and by the thermal pressure gradient in the outer CGM (Oppenheimer 2018), but no such dynamical stability (i.e. HSE) applies to the high-z hot CGM, which is primarily outflowing (Fig. 9).

(vii) The angular momentum spin parameter of the CGM is substantially higher than that of the dark matter at both epochs. The average hot CGM spin parameters are 66 per cent of the cool CGM spin parameters at high z and 87 per cent at low z. Owing to a greater hot CGM mass at low z, the total angular momentum in the low-z hot phase is several times that of the cool phase (Fig. 13).

(viii) Angular momentum vectors are well aligned between the cool and hot CGM at both epochs. The CGM angular momentum is substantially less well aligned with the stellar disc, which may result from gas in the outer CGM being dynamically disconnected from the inner CGM. This does not contradict the existence of the low-z cool CGM often exhibiting co-rotation with the stellar disc (Figs 9 and 14).

(ix) Hot halo profiles have flatter density profiles at low z than at high z. High-z hot haloes are hotter and significantly higher pressure than their low-z counterparts. High-z entropy profiles are rising through most of the halo, while low-z profiles are more isentropic, although with interior positive slopes where hot winds are outflowing (Fig. 15).

Our next paper in this series (Lonardi et al., in preparation) will show that these zoom haloes reproduce key metal absorption line strengths around both star-forming $z \approx 2-3$ and $z \approx 0$ galaxies. While the typical observed column densities do not change much between these two epochs, our main conclusions here show that these two sets of haloes are physically and dynamically distinct. Just as galaxies change significantly over 10 Gyr, the CGM also changes, and it will be crucial to identify observational measures that differentiate high-z and low-z gaseous haloes.

ACKNOWLEDGEMENTS

We wish to thank the anonymous referee for their report that improved and added to this paper. The authors are grateful for valuable discussions with Ryan Horton and Peter Mitchell, and additional calculations by Jonathan Davies and Peter Mitchell. Support for EH was provided by the Undergraduate Research Opportunities Program at the University of Colorado Boulder. BDO was supported through the NASA ATP grant NNX16AB31G and NASA *Hubble* grant *HST*-AR-14308. RAC is a Royal Society University Research Fellow. AJR was supported by a CO-FUND/Durham Junior Research Fellowship under EU grant 609412; and by the Science and Technology Facilities Council [ST/P000541/1]. This work used the DiRAC@Durham facility managed by the Institute for Computational Cosmology on behalf of the STFC DiRAC HPC Facility (http://www.dirac.ac.uk). The equipment was funded by BEIS capital funding via STFC capital grants ST/K00042X/1, ST/P002293/1, ST/R002371/1 and ST/S002502/1, Durham University and STFC operations grant ST/R000832/1. DiRAC is part of the National e-Infrastructure.

DATA AVAILABILITY

All simulations and data outputs from this work are available to the public upon request. Please e-mail benjamin.oppenheimer@colorado.edu if you require simulation snapshot outputs, and ezra.huscher@colorado.edu if you require a specific form of the data presented here.

REFERENCES

Abraham R. G., Tanvir N. R., Santiago B. X., Ellis R. S., Glazebrook K., van den Bergh S., 1996, MNRAS, 279, L47
Adelberger K. L., Steidel C. C., Shapley A. E., Pettini M., 2003, ApJ, 584, 45
Anderson M. E., Churazov E., Bregman J. N., 2016, MNRAS, 455, 227
Asplund M., Grevesse N., Sauval A. J., Scott P., 2009, ARA&A, 47, 481
Behroozi P. S., Wechsler R. H., Conroy C., 2013a, ApJ, 762, L31
Behroozi P. S., Wechsler R. H., Conroy C., 2013b, ApJ, 770, 57

Bogdán Á., Bourdin H., Forman W. R., Kraft R. P., Vogelsberger M., Hernquist L., Springel V., 2017, ApJ, 850, 98
Borthakur S. et al., 2015, ApJ, 813, 46
Bouché N., Lehnert M. D., Aguirre A., Péroux C., Bergeron J., 2007, MNRAS, 378, 525
Bower R. G., Schaye J., Frenk C. S., Theuns T., Schaller M., Crain R. A., McAlpine S., 2017, MNRAS, 465, 32
Bregman J. N., 2007, ARA&A, 45, 221
Burchett J. N. et al., 2015, ApJ, 815, 91
Chen H.-W., 2012, MNRAS, 427, 1238
Correa C. A., Schaye J., Wyithe J. S. B., Duffy A. R., Theuns T., Crain R. A., Bower R. G., 2018, MNRAS, 473, 538
Crain R. A. et al., 2015, MNRAS, 450, 1937
Dalla Vecchia C., Schaye J., 2012, MNRAS, 426, 140
Das S., Mathur S., Gupta A., Nicastro F., Krongold Y., Null C., 2019, ApJ, 885, 108
Davé R., Anglés-Alcázar D., Narayanan D., Li Q., Rafieferantsoa M. H., Appleby S., 2019, MNRAS, 486, 2827
Davies J. J., Crain R. A., McCarthy I. G., Oppenheimer B. D., Schaye J., Schaller M., McAlpine S., 2019, MNRAS, 485, 3783
Davies J. J., Crain R. A., Oppenheimer B. D., Schaye J., 2020, MNRAS, 491, 4462
DeFelippis D., Genel S., Bryan G. L., Nelson D., Pillepich A., Hernquist L., 2020, ApJ, 895, 17
Dekel A., Birnboim Y., 2006, MNRAS, 368, 2
Dubois Y., Peirani S., Pichon C., Devriendt J., Gavazzi R., Welker C., Volonteri M., 2016, MNRAS, 463, 3948
Faerman Y., Sternberg A., McKee C. F., 2020, ApJ, 893, 82
Ford A. B., Oppenheimer B. D., Davé R., Katz N., Kollmeier J. A., Weinberg D. H., 2013, MNRAS, 432, 89
Gatkine P., Veilleux S., Cucchiara A., 2019, ApJ, 884, 66
Hafen Z. et al., 2019, MNRAS, 488, 1248
Hafen Z. et al., 2020, MNRAS, 494, 3581
Hodges-Kluck E. J., Miller M. J., Bregman J. N., 2016, ApJ, 822, 21
Hopkins P. F., 2013, MNRAS, 428, 2840
Johnson S. D., Chen H.-W., Mulchaey J. S., 2015, MNRAS, 449, 3263
Keller B. W., Kruijssen J. M. D., Wadsley J. W., 2020, MNRAS, 493, 2149
Kereš D., Katz N., Weinberg D. H., Davé R., 2005, MNRAS, 363, 2
Kereš D., Katz N., Fardal M., Davé R., Weinberg D. H., 2009, MNRAS, 395, 160
Li J.-T., Wang Q. D., 2013, MNRAS, 428, 2085
Li J.-T., Bregman J. N., Wang Q. D., Crain R. A., Anderson M. E., Zhang S., 2017, ApJS, 233, 20
Miller M. J., Hodges-Kluck E. J., Bregman J. N., 2016, ApJ, 818, 112
Mitchell P. D., Schaye J., Bower R. G., Crain R. A., 2020a, MNRAS, 494, 3971
Mitchell P. D., Schaye J., Bower R. G., 2020b, MNRAS, 497, 4495
Moster B. P., Naab T., White S. D. M., 2013, MNRAS, 428, 3121
Muratov A. L. et al., 2017, MNRAS, 468, 4170
Oppenheimer B. D., 2018, MNRAS, 480, 2963
Oppenheimer B. D., Schaye J., 2013, MNRAS, 434, 1043
Oppenheimer B. D. et al., 2016, MNRAS, 460, 2157 (O16)
Oppenheimer B. D., Segers M., Schaye J., Richings A. J., Crain R. A., 2018a, MNRAS, 474, 4740
Oppenheimer B. D., Schaye J., Crain R. A., Werk J. K., Richings A. J., 2018b, MNRAS, 481, 835
Oppenheimer B. D. et al., 2020a, MNRAS, 491, 2939
Oppenheimer B. D. et al., 2020b, ApJ, 893, L24
Peeples M. S., Werk J. K., Tumlinson J., Oppenheimer B. D., Prochaska J. X., Katz N., Weinberg D. H., 2014, ApJ, 786, 54
Pettini M., Shapley A. E., Steidel C. C., Cuby J.-G., Dickinson M., Moorwood A. F. M., Adelberger K. L., Giavalisco M., 2001, ApJ, 554, 981
Pezzulli G., Cantalupo S., 2019, MNRAS, 486, 1489
Pillepich A. et al., 2018, MNRAS, 473, 4077
Planck Collaboration XVI, 2014, A&A, 571, A16
Rahmati A., Schaye J., Crain R. A., Oppenheimer B. D., Schaller M., Theuns T., 2016, MNRAS, 459, 310
Reid M. J. et al., 2014, ApJ, 783, 130
Richings A. J., Schaye J., Oppenheimer B. D., 2014, MNRAS, 440, 3349
Rosas-Guevara Y., Bower R. G., Schaye J., McAlpine S., Dalla Vecchia C., Frenk C. S., Schaller M., Theuns T., 2016, MNRAS, 462, 190
Rudie G. C., Steidel C. C., Pettini M., Trainor R. F., Strom A. L., Hummels C. B., Reddy N. A., Shapley A. E., 2019, ApJ, 885, 61
Schaller M., Dalla Vecchia C., Schaye J., Bower R. G., Theuns T., Crain R. A., Furlong M., McCarthy I. G., 2015, MNRAS, 454, 2277
Schaye J., Dalla Vecchia C., 2008, MNRAS, 383, 1210
Schaye J. et al., 2010, MNRAS, 402, 1536
Schaye J. et al., 2015, MNRAS, 446, 521
Springel V., 2005, MNRAS, 364, 1105
Steidel C. C., Giavalisco M., Pettini M., Dickinson M., Adelberger K. L., 1996, ApJ, 462, L17
Steidel C. C., Erb D. K., Shapley A. E., Pettini M., Reddy N., Bogosavljević M., Rudie G. C., Rakic O., 2010, ApJ, 717, 289
Stern J., Fielding D., Faucher-Giguère C.-A., Quataert E., 2019, MNRAS, 488, 2549
Stevens A. R. H., Lagos C. d. P., Contreras S., Croton D. J., Padilla N. D., Schaller M., Schaye J., Theuns T., 2017, MNRAS, 467, 2066
Stewart K. R., Kaufmann T., Bullock J. S., Barton E. J., Maller A. H., Diemand J., Wadsley J., 2011, ApJ, 738, 39
Stewart K. R. et al., 2017, ApJ, 843, 47
Stocke J. T., Keeney B. A., Danforth C. W., Shull J. M., Froning C. S., Green J. C., Penton S. V., Savage B. D., 2013, ApJ, 763, 148
Terrazas B. A. et al., 2020, MNRAS, 493, 1888
Thob A. C. R. et al., 2019, MNRAS, 485, 972
Truong N. et al., 2020, MNRAS, 494, 549
Tumlinson J. et al., 2011, Science, 334, 948
Turner M. L., Schaye J., Steidel C. C., Rudie G. C., Strom A. L., 2014, MNRAS, 445, 794
Turner M. L., Schaye J., Crain R. A., Rudie G., Steidel C. C., Strom A., Theuns T., 2017, MNRAS, 471, 690
van de Voort F., Schaye J., 2012, MNRAS, 423, 2991
van Dokkum P. G. et al., 2008, ApJ, 677, L5
Voit G. M., Kay S. T., Bryan G. L., 2005, MNRAS, 364, 909
Wendland H., 1995, Adv. Comput. Math., 4, 389
Werk J. K., Prochaska J. X., Thom C., Tumlinson J., Tripp T. M., O'Meara J. M., Peeples M. S., 2013, ApJS, 204, 17
Wiersma R. P. C., Schaye J., Smith B. D., 2009a, MNRAS, 393, 99
Wiersma R. P. C., Schaye J., Theuns T., Dalla Vecchia C., Tornatore L., 2009b, MNRAS, 399, 574

This paper has been typeset from a TEX/LATEX file prepared by the author.